Quarterly Report for

Contract DE-FG07-02ID14418

Stanford Geothermal Program

April-June 2003

Table of Contents

1. STEAM-WATER RELATIVE PERMEABILITY IN FRACTURES

This project is being conducted by Research Assistant Chih-Ying Chen, Senior Research Engineer Kewen Li and Prof. Roland Horne. The goal of this research has been to compare steam- and air-water transport through fractured media and gain better understanding of the behaviors of relative permeability in fractures. Air-water (or nitrogen-water) relative permeabilities are often used for geothermal reservoir simulations while steam-water relative permeabilities in fractures are rarely measured owing to difficulties and complexities of steam-water experiments. A novel and accurate methodology was developed to capture the unstable nature of the steam-water flow in a smooth-walled fracture. Repeatable results were obtained and show that steam-water relative permeabilities are different from nitrogen-water relative permeabilities. The average steam-water relative permeabilities show less phase interference. Also, comparing with previous research into air-water relative permeabilities in fractures, both average steam- and nitrogen-water relative permeabilities were seen to behave closer to the X-curve.

1.1 THEORETICAL BACKGROUND

Multiphase flow is an important mechanism in geothermal reservoirs, which are complex systems of porous and fractured media. Complete understanding of geothermal fluid flow requires knowledge of flow in both media. Normally, fractures are the main conduits for fluid. In geothermal reservoirs, the fluids, steam and water, are both derived from the same substance but in different phases. The phase change during steam-water flow is a physical phenomenon that does not occur in the multiphase flow of distinct fluids such as air and water, hence the multiphase flow properties are likely to differ. At present, the governing flow mechanism for boiling multiphase flow in fractures is still undetermined. There are two approaches commonly used to model multiphase flow in fractures, the porous medium approach and the equivalent homogeneous single-phase approach.

The porous medium approach treats fractures as connected two-dimensional porous media. In this model, a pore space occupied by one phase is not available for flow for the other phase. A phase can move from one position to another only upon establishing a continuous flow path for itself. As in porous media, the competition for pore occupancy is described by relative permeability and governed by Darcy's law. Darcy's law for single-phase liquid system is:

$$u_l = \frac{k_{abs}(p_i - p_o)}{\mu_l L} \tag{1.1}$$

where subscript l stands for the liquid phase, i for inlet and o for outlet; μ, p, L, u, k_{abs} are the viscosity, pressure, fracture length, Darcy flow velocity and absolute permeability respectively. The Darcy flow velocity is equal to

$$u = \frac{q}{bw} \tag{1.2}$$

with q as the volumetric flow rate, b the fracture aperture and w as the fracture width. The absolute permeability of a smooth-walled fracture is a function only of the fracture aperture (Witherspoon et al., 1980) as described in the relationship:

$$k_{abs} = \frac{b^2}{12} \tag{1.3}$$

For liquid phase in two-phase flow, Eq. 1.1 becomes

$$u_l = \frac{k_{abs} k_{rl} (p_i - p_o)}{\mu_l L} \tag{1.4}$$

where k_{rl} is the relative permeability of the liquid phase.

Similarly, Darcy's law derived for single-phase isothermal gas flow in porous media (Scheidegger, 1974) is:

$$u_g = \frac{k_{abs} (p_i^2 - p_o^2)}{2\mu_g L p_o} \tag{1.5}$$

with the subscript *g* pertaining to the gas phase.

In two-phase flow, Eq. 1.5 becomes

$$u_g = \frac{k_{abs} k_{rg} (p_i^2 - p_o^2)}{2\mu_g L p_o} \tag{1.6}$$

with k_{rg} as the gas relative permeability. The sum of the k_{rl} and k_{rg} indicates the extent of phase interference. A sum of relative permeabilities equal to one means the absence of phase interference. Physically this implies that each phase flows in its own path without impeding the flow of the other. The lower is the sum of the relative permeabilities below 1, the greater is the phase interference.

Relative permeability functions are usually taken to be dependent on phase saturation. The two most commonly used expressions for relative permeability for homogeneous porous media are the X-curve and the Corey curve (Corey, 1954). The X-curve defines relative permeability as a linear function of saturation:

$$k_{rl} = S_l \tag{1.7}$$

$$k_{rg} = S_g \tag{1.8}$$

where S_l and S_g are the liquid and gas saturation respectively. The Corey curves relate relative permeability to the irreducible or residual liquid and gas saturation, S_{rl} and S_{rg} :

$$k_{rl} = S^{*4} \tag{1.9}$$

$$k_{rg} = (1 - S^*)^2 (1 - S^{*2}) \tag{1.10}$$

$$S^* = (S_l - S_{rl}) / (1 - S_{rl} - S_{rg}) \tag{1.11}$$

The equivalent homogeneous single-phase approach treats flow through fractures as a limiting case of flow through pipes. In this model, phase velocities in the fracture are equal and capillary forces are negligible. A continuous flow path is not required for movement of each phase. A phase can be carried along by one phase as bubbles, slug or other complex structures. As in pipes, flow can be described by the concept of friction factors and using averaged properties (Fourar et al., 1993):

$$\frac{(p_i - p_o)}{L} = \frac{\Pi f \rho_m V_m^2}{2A} \tag{1.12}$$

where Π is the fracture perimeter, A is the cross sectional area to flow, ρ_m average density and V_m as average flow velocity. The average density is described by:

$$\rho_m = \frac{\rho_g q_g + \rho_l q_l}{q_g + q_l} \tag{1.13}$$

The average flow velocity is equal to:

$$V_m = \frac{q_g + q_l}{A} \tag{1.14}$$

The friction factor, f, is derived empirically as a function of the averaged Reynolds number calculated by:

$$N_{\mathrm{Re}} = \frac{2bV_m\rho_m}{\mu_m} \tag{1.15}$$

with μ_m as average viscosity:

$$\mu_m = \frac{\mu_g q_g + \mu_l q_l}{q_g + q_l} \tag{1.16}$$

There are several expressions used to relate friction factor and Reynold's number. The commonly used one for flow through fracture is the generalized Blasius form (Lockhart and Martinelli, 1949):

$$f = \frac{C}{N_{\mathrm{Re}}^n} \tag{1.17}$$

with C and n as constants derived from experimental data.

According to the results from Diomampo (2001), nitrogen-water flow through fractures is described more appropriately by using the porous medium (relative permeability) approach based on the observations of the multiphase flow behavior. However in the steam-water case, the applicability of the two models for multiphase flow through fractures is still undetermined. From the preliminary results in this research, the steam-water flow shows a different behavior from the nitrogen-water case reported by Diomampo (2001).

1.2 LITERATURE REVIEW

The fluids in geothermal reservoirs, steam and water, are both derived from the same substance. However, they form different phases. The phase change during steam-water multiphase flow has made it difficult to investigate steam-water relative permeability. Even in multiphase flow without boiling, few published data are available for two-phase flow in fractures. Most of the studies have been done for air-water systems or for water-oil systems.

Previous work on multiphase flow in fractures includes Romm's (1966) experiment with kerosene and water through an artificial parallel-plate fracture lined with strips of polyethylene or waxed paper. Romm found a linear relationship between permeability and saturation, $S_w = k_{rw}$, $S_{nw} = k_{rnw}$ such that $k_{rw}+k_{rnw} = 1$ which represents the X-curve behavior. Fourar et al. (1993) artificially roughened glass plates with beads and flowed an

air-water mixture between them. Fourar and Bories (1995) did similar experiments using smooth glass plates and clay bricks. Both studies observed flow structures like bubbles, annular and fingering bubbles comparable to flow in pipes and depicted flow in fractures to be better correlated using the equivalent homogeneous single-phase model. Pan et al. (1996) observed the identical flow structures in their experiments with an oil-water system. They observed that a discontinuous phase can flow as discrete units along with the other phase. Pan et al. (1996) also found their experimental pressure drop to be better predicted by a homogenous single-phase model. All of these experiments showed significant phase interference at intermediate saturations.

Pruess and Tsang (1990) conducted numerical simulation of flow through rough-walled fractures. They modeled fractures as two-dimensional porous media with apertures varying with position. Their study showed the sum of the relative permeabilities to be less than 1, the residual saturation of the nonwetting phase to be large and phase interference to be greatly dependent on the presence or absence of spatial correlation of aperture in the direction of flow. Persoff et al. (1991) did experiments on gas and water flow through rough-walled fractures using transparent casts of natural fractured rocks. The experiment showed strong phase interference similar to the flow in porous media. The relative permeability data of Persoff (1991) and Persoff and Pruess (1995) for flow through rough-walled fractures were compared in Horne et al. (2000) against commonly used relative permeability relations for porous media, the X-curve and Corey curve, as shown in Figure 1.1. Diomampo (2001) performed experiments of nitrogen and water flow through both smooth- and rough-walled artificial fractures, leading to results that are also included in Figure 1.1.

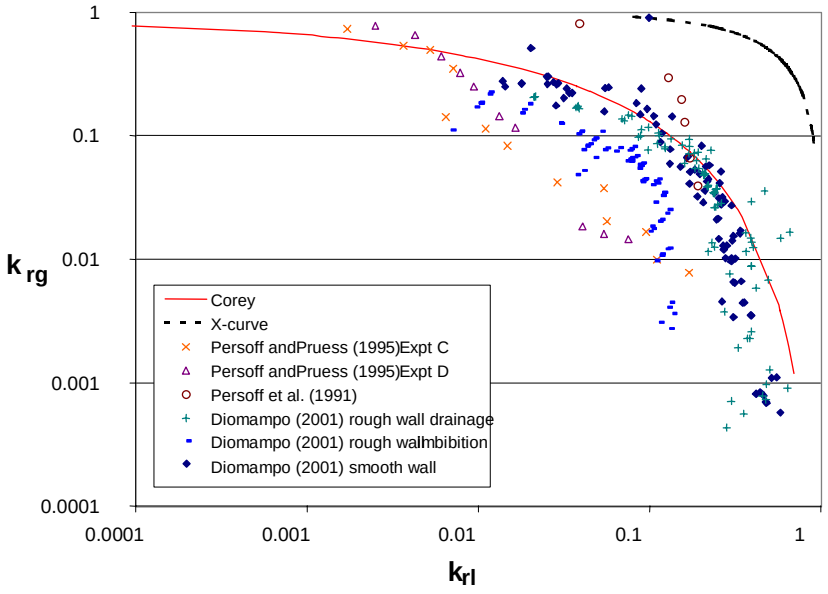

Figure 1.1: Compendium of previous measurements of air-water relative permeabilities in fractures (from Diomampo, 2001).

In the experiments of both Persoff (1991) and Persoff and Pruess (1995), flow of a phase was characterized by having a localized continuous flow path that is undergoing blocking and unblocking by the other phase. Recent parallel plate experiments by Su et al. (1999)

illustrate the same flow mechanism of intermittent localized fluid flow. Kneafsy and Pruess (1998) observed similar intermittent flow in their experiments with pentane through various parallel plate models made from glass, sandblasted glass or transparent fracture replicas. Diomampo (2001) also observed the intermittent phenomenon in her experiments. Furthermore, the results from Diomampo (2001) conform mostly to the Corey type of relative permeability curve (Figure 1.1). This suggests that flow through fractures can be analyzed by treating it as a limiting case of porous media flow and by using the relative permeability approach. These observations are contrary to the findings of Fourar et al (1993), Fourar and Bories (1995), and Pan et al. (1996).

Presently, the flow mechanism and the characteristic behavior of relative permeability in fractures are still not well determined. Issues such as whether a discontinuous phase can travel as discrete units carried along by another phase or will be trapped as residual saturation as in porous medium are unresolved. The question of phase interference i.e. whether the relative permeability curve against saturation is described by an X-curve, Corey or some other function, is still unanswered. The main objective of this study was to contribute to the resolution of these issues. Experiments on flow through smooth-walled and rough-walled fractures without boiling have been conducted by Diomampo (2001), who initially established a methodology for flow characterization and relative permeability calculation for nitrogen-water flow. A more sophisticated and reliable methodology was modified and used for relative permeability experiments in steam- and nitrogen-water flows in this research.

1.3 EXPERIMENTAL METHODOLOGY

The steam-water flow experiment is more complex than air-water experiment conducted previously by Diomampo (2001). The steam-water flow experiment has to be performed at high temperature, and there is a fundamental difficulty measuring how much of the fluid flows as steam and how much as liquid. The whole experiment system is illustrated in Figure 1.2, which shows the deaerated water supply, the fracture apparatus (inside the air bath), data acquisition system, and digital image recording (also see Figure 1.18).

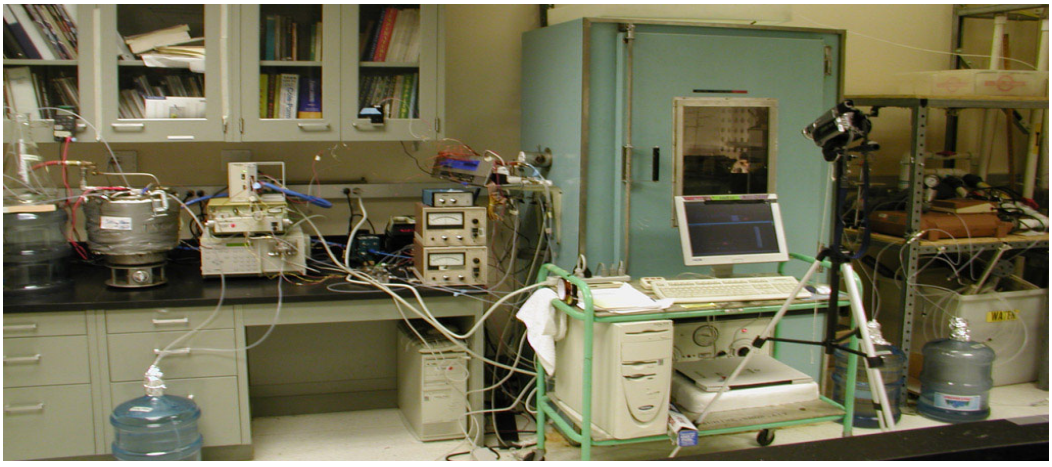

Figure 1.2: Picture of steam-water flow through fracture apparatus.

Fracture Apparatus Description

The fracture is created by a smooth glass plate on top of an aluminum plate, confined by a metal frame bolted to the bottom plate. The frame was designed to improve the seal and to prevent deformation of the glass due to system pressure. The metal frame has several windows and a mirror attached to it for flow visualization (see Figure 1.3 and Figure 1.4.)

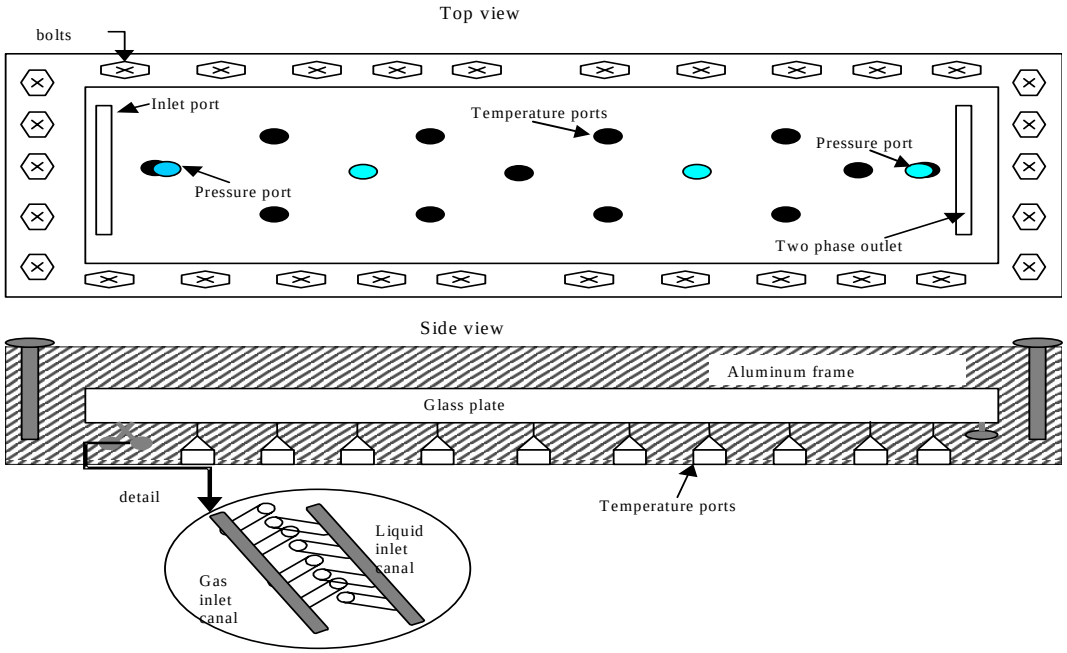

Figure 1.3: Schematic diagram of fracture apparatus.

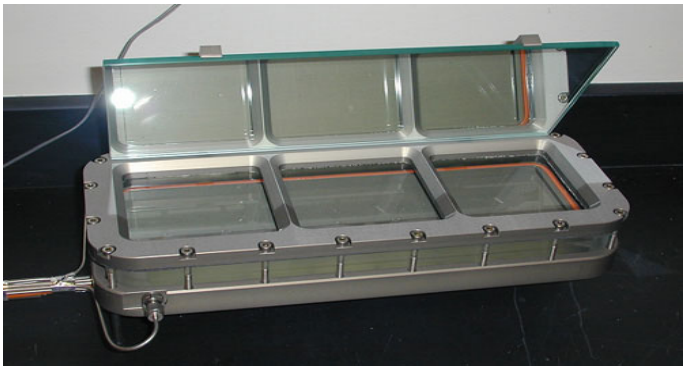

Figure 1.4: Picture of fracture apparatus.

An O-ring (Viton 1/8" thick #2-272) was placed in between the glass and aluminum plate as a seal (see orange color lining in Figure 1.4). Placing this O-ring in the channel was not sufficient to provide a good seal because the channel was custom made in width and length. Thinly cut rubber sheets were placed at the outer boundary to push the O-ring to the sides of the aluminum plate. These provided an excellent seal when compressed with the glass and metal frame. Since the O-ring is cylindrical in shape and the aluminum plate is rectangular, there is a narrow channel in between the O-ring and the plate when squeezed together. A thin lining of copper-based adhesive (Permatex Ultra Copper) was

applied to fill this channel. It is important to eliminate this channel for it serves as an easy conduit for the fluid to pass through instead of the fracture.

The phases enter the fracture through two separate canals. Each canal has several ports drilled in a way that they align on the surface (see Figure 1.3). In the nitrogen-water experiments both entry canals were used, but in the steam-water experiments only water was injected and the steam was created by boiling within the fracture itself. The surface of the fracture apparatus was designed such that there is an available 12 inch by 4 inch space for flow. Throughout this flow area, tiny temperature ports the size of needles were drilled. Needle-size ports were drilled so as to minimize surface discontinuity. A pressure port was drilled at each end of the flow path. The two-phase fluid exits through a single outlet. The apparatus was designed to be of sufficient length that end effects only influence a small part of the flow window – experimental observations have confirmed this to be true.

Pressure Transducers

Low-range differential transducers were used to measure the pressure drop through the fracture, as well as the intermediate pressure and the two-phase outlet pressure. Two liquid differential transducers (Validyne Transducer, model DP-15, range 0-2psi) were attached to four pressure ports inside the fracture to measure the pressure drop through the fracture. Another transducer (Validyne Transducer, model DP-15, range 0-5psi) was attached to the middle point of the fracture. The fourth transducer (Validyne Transducer, model DP-15, range 0-5psi) was attached to the two-phase outlet of the fracture apparatus. These transducers send electrical signals to the SCXI-1000 data acquisition device, which was monitored using the LabView® programmable virtual instrument software. The complete improved measurement configuration in the fracture apparatus is shown in Figure 1.5(a) and (b).

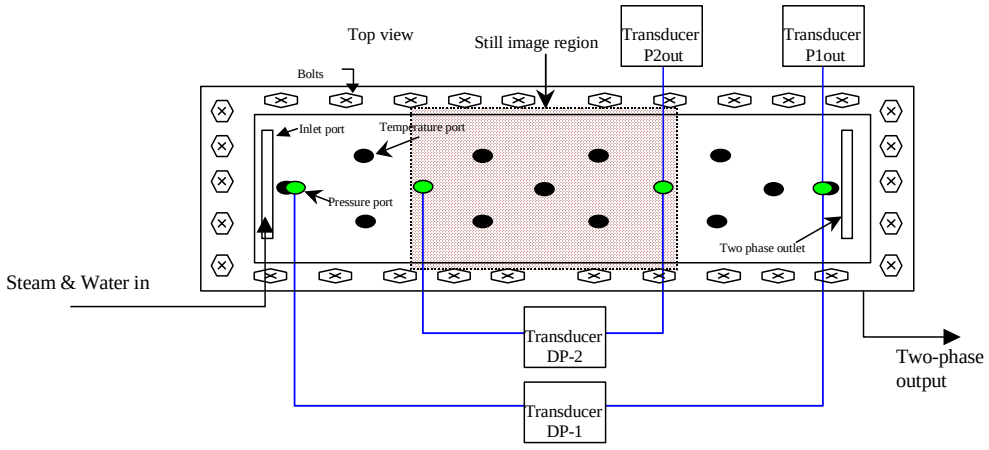

(a) Steam-water steady experiments.

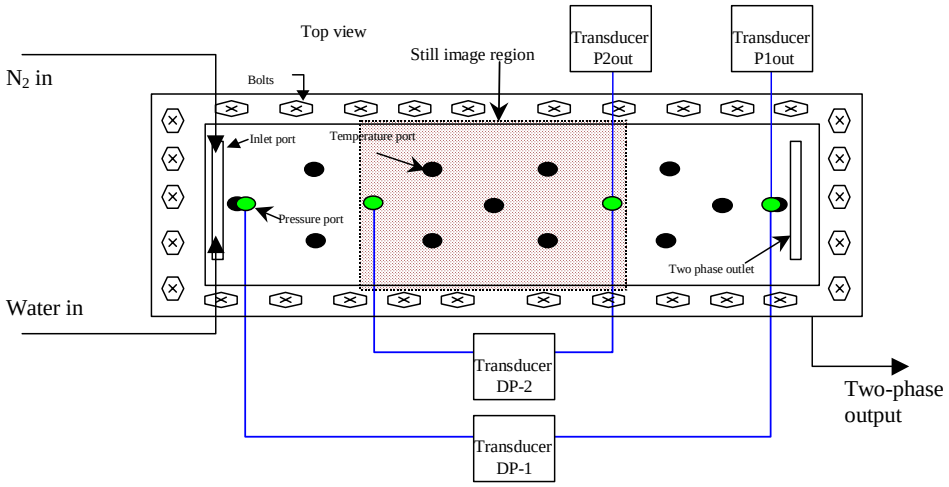

(b) Nitrogen-water steady experiments.

Figure 1.5: Schematic diagrams of pressure measurements in fracture apparatus in steady experiments. (a) Steam-water steady experiments. (b) Nitrogen-water steady experiments.

Capillary end effect was another issue that influenced the previous unsteady experiment. In the current experiments, two new pressure ports were drilled along the fracture for intermediate pressure difference measurement to minimize capillary end effect and to facilitate intermediate absolute pressure measurement through the fracture. Another issue that affects the pressure measurement is the phase transformation inside the pressure tubing. Since experiments were conducted at a temperature nearly boiling point of water, the water-filled pressure tubing connected to the pressure transducers has a tendency to boil. This means both liquid water and gas would coexist inside the pressure tubing. This situation can be illustrated in Figure 1.6. Insensitive and erratic pressure response was obtained due to the different compressibility in water and gas and the solubility of gas. An additional outer cooling tubing was added to cool down the pressure tubing to minimize this two-phase phenomenon inside the pressure tubing. This cooling tubing is expected to quench the pressure tubing and maintain the content inside the pressure tubing in the liquid phase (water). The new plumbing of the pressure measurement is shown in Figure 1.7.

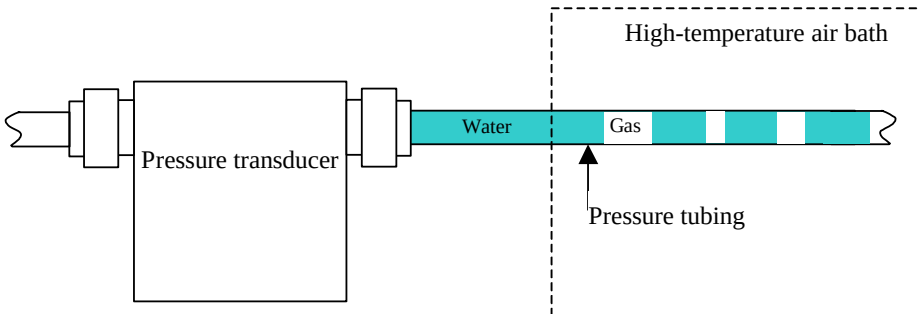

Figure 1.6: Two-phase problem inside the pressure tubing.

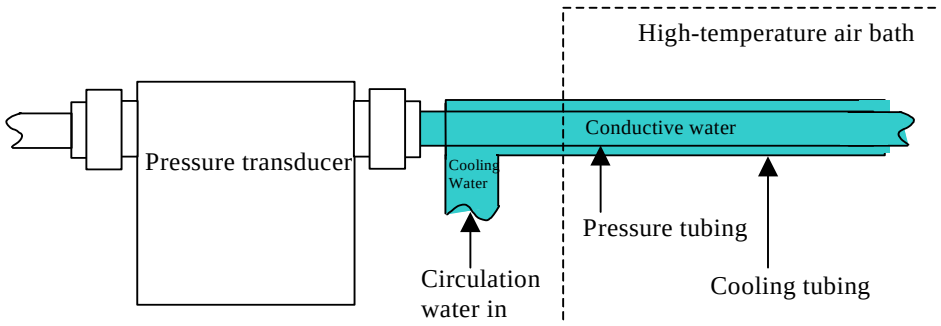

Figure 1.7: Improved plumbing of the pressure measurement to reduce two-phase problem shown in Figure 1.6.

Fractional Flow Ratio Detector (FFRD)

One of the main challenges of the steam-water flow experiment was to measure the steam and water flow rates, since there is phase transition occurring when steam and water flow through the fracture. Therefore using flow meters to measure the rate of each phase becomes inappropriate, because it is always impossible to separate steam from water without any mass loss or gain. To overcome this situation, an in-situ fractional flow ratio detector (FFRD) was designed and constructed as shown in Figure 1.8. The principal of the FFRD is that different phases will have different refractive indices. A phototransistor (NTE 3038, NPN-Si, Visible, Vcbo 25V, Ic 20mA, Pd 50 mW, response time 1.5 μs) was installed inside the FFRD, producing different voltages when sensing different strengths of light. The water phase produces a higher voltage when flowing through the FFRD. In order to minimize the heat loss between the outlet of the fracture apparatus and the FFRD, the FFRD device was installed as close to the outlet of the fracture as possible (about 5cm distance). An example of the FFRD response signal during testing is shown in Figure 1.9.

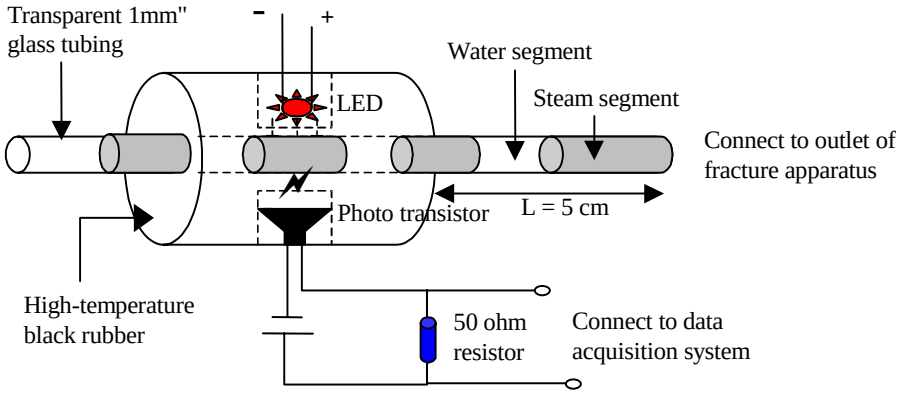

Figure 1.8: Schematic of fractional flow ratio detector (FFRD).

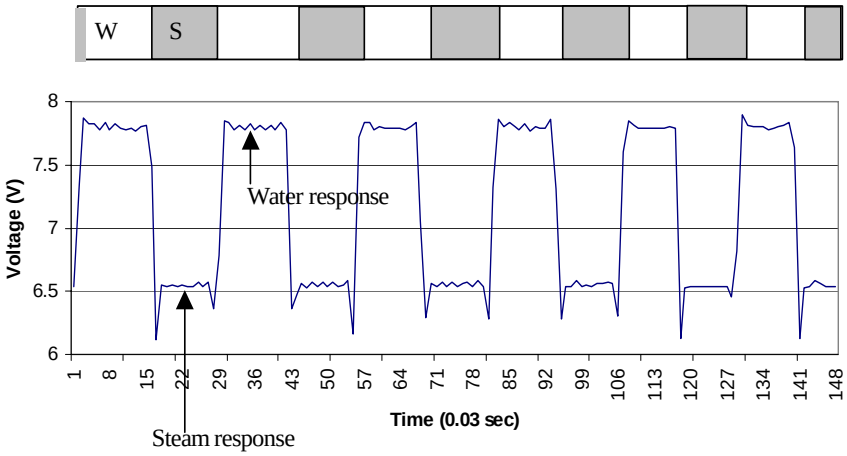

Figure 1.9: The signal of steam and water detected from fractional flow ratio detector.

Once the steam and water responses are obtained from the FFRD, the statistical histogram is plotted and the steam and water phase flow ratios are obtained by determining the threshold of the histogram. This is shown in Figure 1.10 and Table 1.1.

Table 1.1: The analysis results of steam and water fractional flow ratios from Figure 1.9.

Bin	*Frequency*	Discrimination
6.2	287	Steam
6.4	603	Steam
6.6	7021	Steam
6.8	600	Steam
7	110	Steam
7.2	20	Threshold
7.4	146	Water
7.6	400	Water
7.8	3810	Water
8	3462	Water
More	0	

Steam Total	8631
Water Total	7828
Grand total	16459

Fractional flow	
Steam	0.5243939
Water	0.4756061

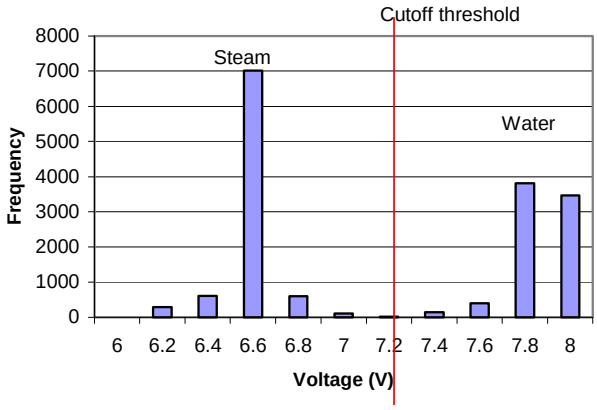

Figure 1.10: The histogram obtained from Figure 1.9.

The diameter of the FFRD tubing plays an important role in the accuracy of the f_w measurement under low f_w conditions. Here, we exam the effect of the FFRD tubing's size by using two different diameter of FFRD tubing.

First, a wider transparent glass tubing (3 mm OD, 1.4 mm ID) was installed. A new, high-speed data acquisition board (NI PCI-6023E) was also installed in the data acquisition computer. This replacement increased the data logging frequency from 50Hz to 250Hz. The calibration of water-phase flow ratio is shown in Figure 1.11. Though this replacement improved the f_w detection limit of the FFRD from 0.01 to around 0.005, f_w values show erratic and inconsistent behavior when f_w is less than 0.005, as shown in Figure 1.11(b). In order to find the solution to this problem, we observed the actual flow phenomena through the FFRD tubing, and did a preliminary classification of flow patterns correspond to logged FFRD signals. Flow patterns inside the FFRD tubing can be classified into four phenomena. With the increasing of the gas rate, the four phenomena are: segment flow, mostly segment flow, mostly droplet flow, and droplet flow. Cartoons of these four flow patterns are shown in Figure 1.12. The FFRD signals obtained from these four patterns are shown in Figure 1.13.

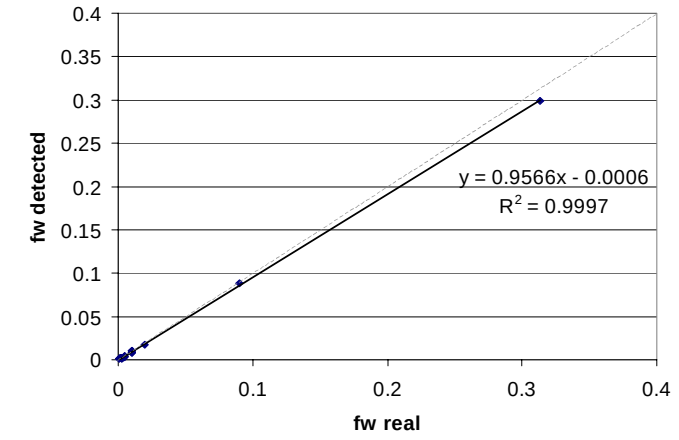

(a)

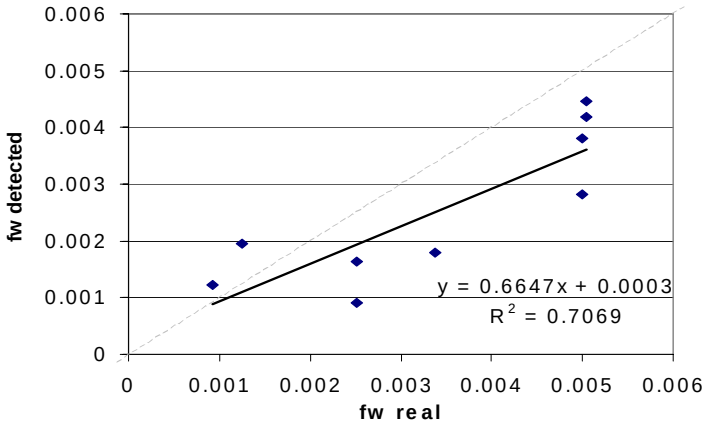

(b)

Figure 1.11:FFRD calibration with tubing ID: 1.4mm, (a) large scale, (b) small scale.

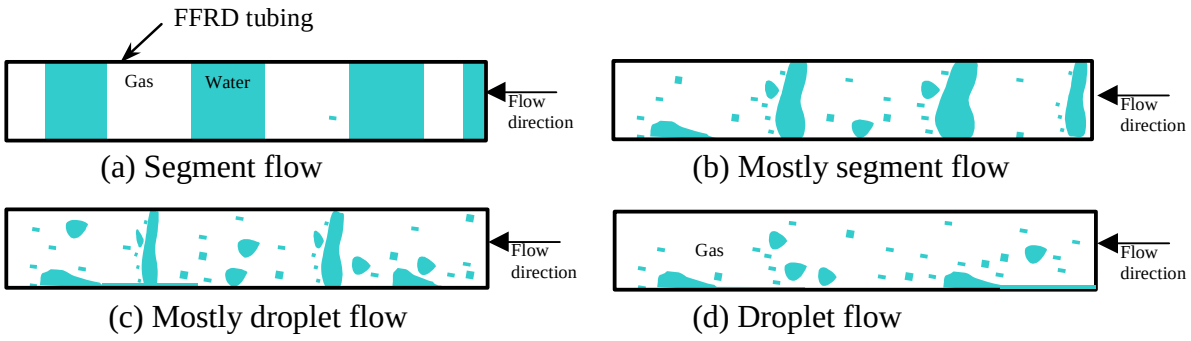

(a) Segment flow (b) Mostly segment flow

(c) Mostly droplet flow (d) Droplet flow

Figure 1.12: Flow pattern cartoons observed from FFRD tubing, (a) segment flow signal, (b) mostly segment flow signal, (c) mostly droplet flow signal and (d) pure droplet flow signal.

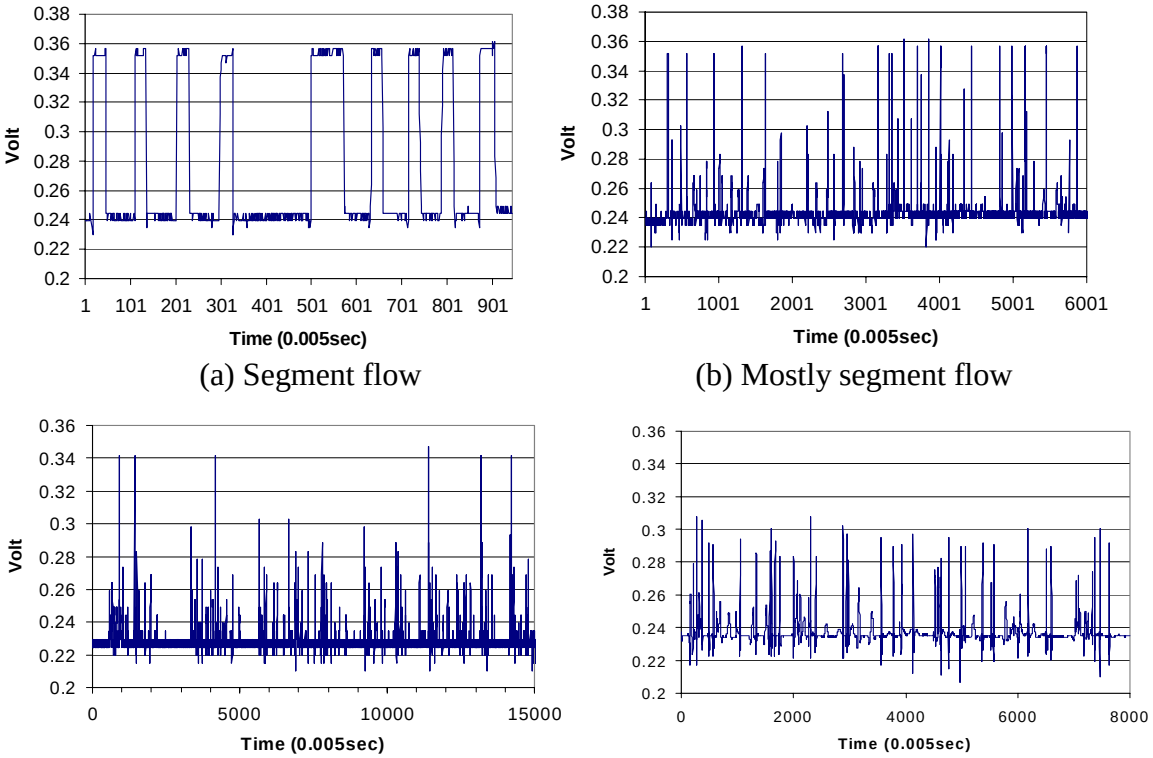

(a) Segment flow (b) Mostly segment flow

(c) Mostly droplet flow (d) Droplet flow

Figure 1.13: FFRD signals correspond to flow patterns shown in Figure 1.12, (a) segment flow signal, (b) mostly segment flow signal, (c) mostly droplet flow signal and (d) pure droplet flow signal.

After analyzing all the FFRD signals obtained by using the 1.4mm ID FFRD tubing, the approximate flow pattern map was drawn (Figure 1.14). Comparing Figure 1.14 and Figure 1.11, we discovered that when f_w is less than 0.005, the flow pattern turns to the pure droplet flow. The more the droplet flow, the more error would be obtained in FFRD detection. Droplets inside the tubing reflect and refract the light from the LCD source randomly, hence the signal attenuation becomes nonlinear. Figure 1.11(b) shows this inaccurate indication due to the droplet flow.

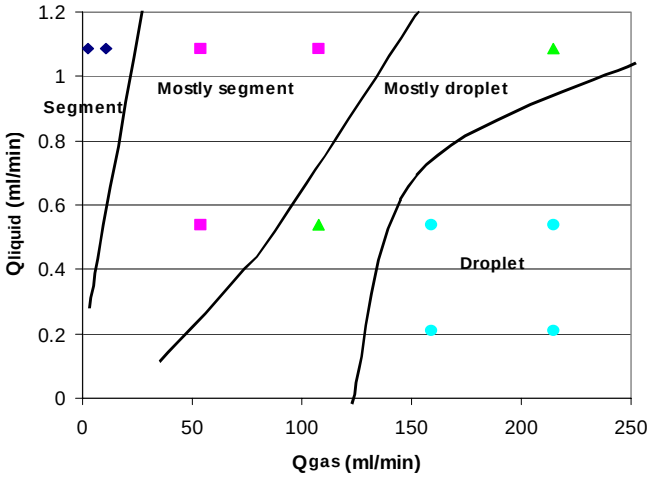

Figure 1.14: Flow pattern map developed from FFRD signal response by using 1.4mm FFRD tubing.

The major factor that controls the flow pattern is FFRD tubing diameter. To avoid the droplet flow, a narrower tubing could be used; however, the narrower the tubing, the more pressure drop throughout the FFRD and the more capillary effect. To maintain an appropriately small pressure drop, keep the tubing size small, and minimize the capillary effect, a new FFRD tubing with 1mm inner diameter and wide-open ends was redesigned to replace the original FFRD tubing (1.4mm) to achieve more segment flow instead of droplet flow inside the FFRD tubing under high flow rates. The schematic of this bell-end tubing is shown in Figure 1.15.

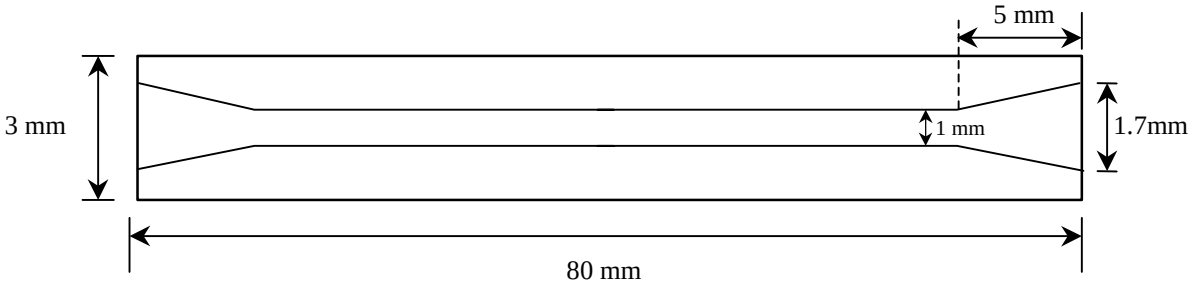

Figure 1.15: Bell-end FFRD tubing (ID=1.0mm, OD=3.0mm, Length=80mm)

The same high-speed data logging program which could reach 250Hz logging frequency was used. Also a more stable DC power supply was installed to avoid signal drift and fluctuation. The new calibration of the FFRD with all the improvements is shown in Figure 1.16 and the new flow pattern map obtained from FFRD signals in different phase-rate ratios is shown in Figure 1.17. Comparing Figure 1.16(b) with Figure 1.11(b), a more accurate measurement of fractional flow in two-phase flow is achieved. This improvement can be explained easily by comparing the flow pattern map in Figure 1.17 with that in Figure 1.14. There is no pure droplet flow region by using this narrower tubing. This increases the accuracy of FFRD logging.

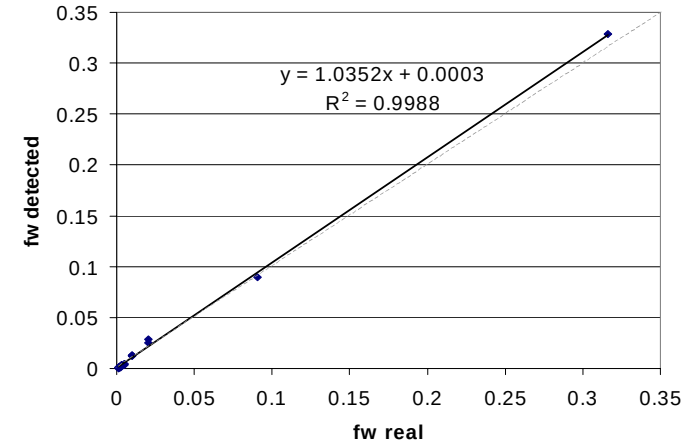

(a)

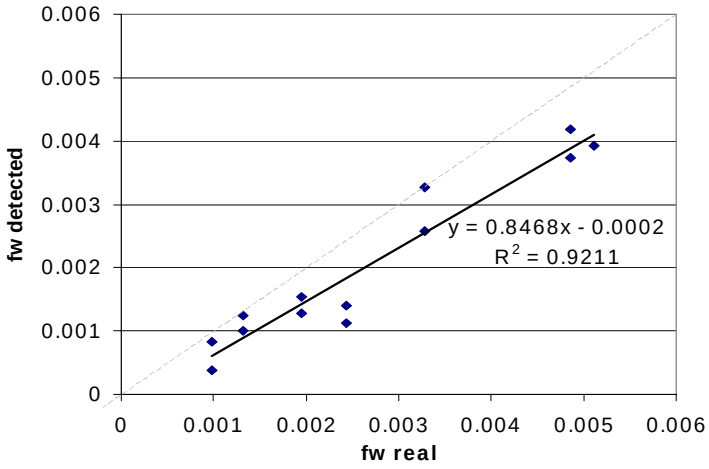

(b)

Figure 1.16:FFRD calibration with tubing ID: 1.0mm, (a) large scale, (b) small scale.

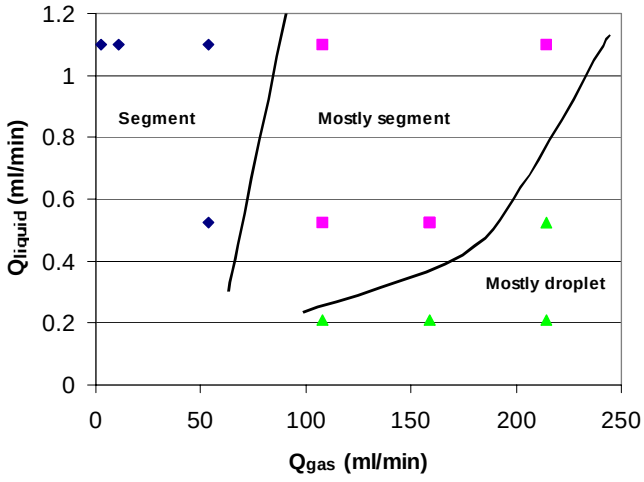

Figure 1.17: Flow pattern map developed from FFRD signal response by using 1.0mm, bell-end FFRD tubing.

1.4 CONTROL AND MEASUREMENT TECHNIQUES

There are two methods available to produce steam-water flow inside the fracture. One method is by injecting steam and water separately into the apparatus. The steam would be produced using a steam generator inside the air bath to boil steam from deaerated water. The other method is by injecting only deaerated water into the apparatus, after which the steam phase is produced by adjusting either pressure or temperature in the fracture. Since the steam quality from the steam generator is hard to control, the heat loss from the steam generator to the fracture apparatus is hard to determine, and there is a significant phase transformation at the moment when the injected steam and water meet in the inlet port, the latter method was used in this experiment.

The two factors that control the steam production are temperature and pressure. According to experience, adjusting pressure requires less equilibration time than adjusting temperature. To facilitate pressure adjustment, a physical back-pressure device was connected to the outlet of the apparatus to constrain the pressure inside the fracture to a specific value. For water, a meter pump (Dynamax, SD-200) controlled the rate of injection. The water used in the experiment needs to be deaerated almost completely. To reach this quality, distilled water was evacuated using a vacuum pump for 2 hours, and then the water was boiled to achieve a low dissolved-gas condition. This distilled, deaerated water was used as the injection fluid. Figure 1.18 shows a schematic diagram of this configuration.

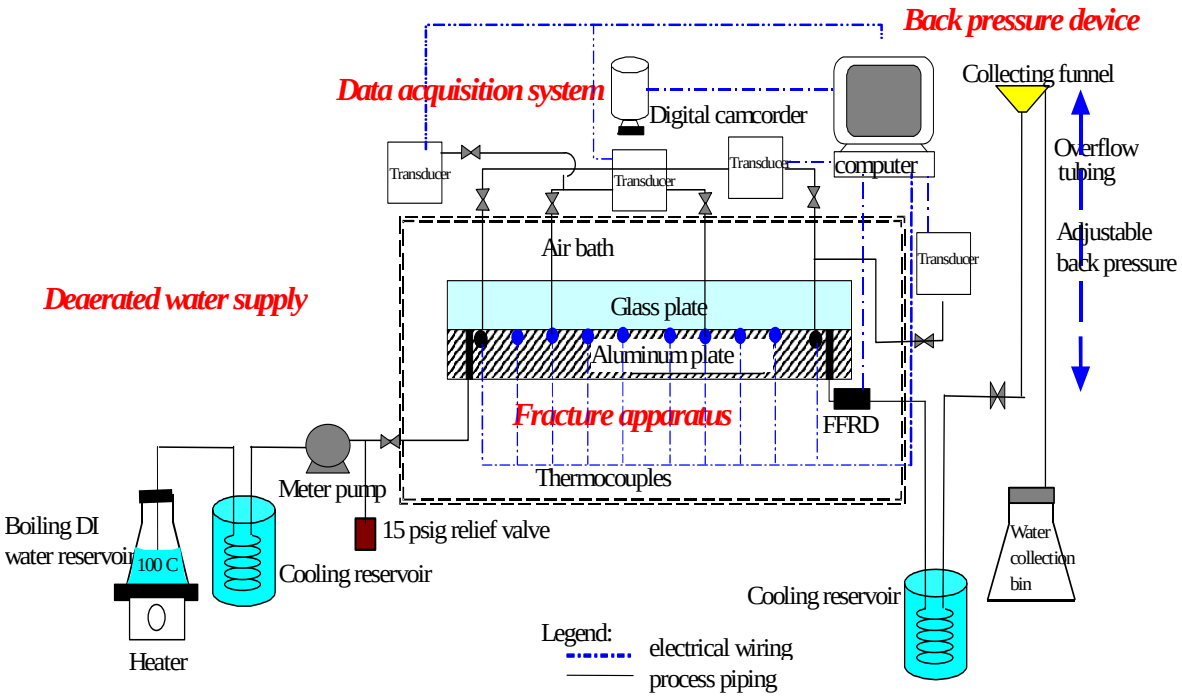

Figure 1.18: Process flow diagram for steam-water experiment.

Flow rates, q_w and q_s

For steam and water rates measurement, the fractional flow ratio detector (FFRD) was used to measure the outlet steam and water fractional flow ratio, f_s and f_w.

$$f_s = \frac{q_{out,s}}{q_{out,t}} \tag{1.18}$$

$$f_w = \frac{q_{out,w}}{q_{out,t}} \tag{1.19}$$

where $q_{out,s}$ is the output steam flow rate, $q_{out,w}$ is the output water flow rate, and $q_{out,t}$ is the output total flow rate. Once f_s and f_w are obtained, it is easy to evaluate $q_{out,s}$ and $q_{out,w}$ by using mass balance if a steady-state condition is reached. In order to catch the fast and unsteady steam and water segment in the outlet tubing, The FFRD was connected to the SCXI-1000 data acquisition device incorporating NI PCI-6023E, high-speed DAQ board, which can reach 250Hz maximum sampling frequency.

Once fractional flows are known, the steam and water flow rate can be calculated according to the mass balance under the assumption of steady state. The mass balance equation is:

$$m_{in} = q_{in,t}\rho_{w,at104^o c} = m_{out} = m_{out,w} + m_{out,s} = q_{out,t}(f_w\rho_{w,at104^o c} + f_s\rho_{s,at104^o c}) \tag{1.20}$$

where, m_{in}, m_{out} stand for the input and output mass, $q_{in,t}$ and $q_{out,t}$ stand for input and output volumetric flow rates, ρ is the density, and f_s and f_w are steam and water fractional flows.

If f_s and f_w are known from FFRD data, the total output flow rate, $q_{out,t}$, can be obtained from Eq. 1.20:

$$q_{out,t} = \frac{m_{in}}{f_w\rho_w + f_s\rho_s} \tag{1.21}$$

The end-point steam and water flow rates are:

$$q_{out,w} = f_w q_{out,t} = f_w \frac{m_{in}}{f_w\rho_w + f_s\rho_s} \tag{1.22}$$

$$q_{out,s} = f_s q_{out,t} = f_s \frac{m_{in}}{f_w\rho_w + f_s\rho_s} \tag{1.23}$$

Since the flow rates obtained are end-point flow rates, they can represent true flow rates under steady-state conditions. If the flow is in an extremely unsteady state, some mixed phase response will occur in the FFRD, and the flow rates calculated will become incorrect. However, if the flow is in quasisteady state (i.e. the steam or water flow rate increases at a fairly slow rate), flow rates obtained by this method should approximate the real flow rates except for a short delay of the phase response.

Saturation

Still images were extracted from digital video recorded during experiments. The data gathered from the video were correlated with the Labview data through the time read from the LCD monitor. Figure 1.19 shows a typical video image taken from the experiments.

From the still image shown in Figure 1.19, saturation was computed by measuring the area that each phase occupied. The photographs were processed in a Matlab® program. The program first cuts the photograph to display just the image of the flow area. Using this cut image, the program does quadratic discriminant analysis (QDA) to group the pixels of the picture into three groups: the water phase, steam phase and the frame. The grouping is based on color differences. Saturation is calculated as total pixels of the liquid group over the sum of the steam and liquid groups. Figure 1.20 is a gray-scaled image produced by the QDA program from the original cut photograph (Figure 1.19). The accuracy of the program in calculating the saturation can be related to the similarity in details of the gray scale image to the true image. From the figure, it can be said that the program has good accuracy.

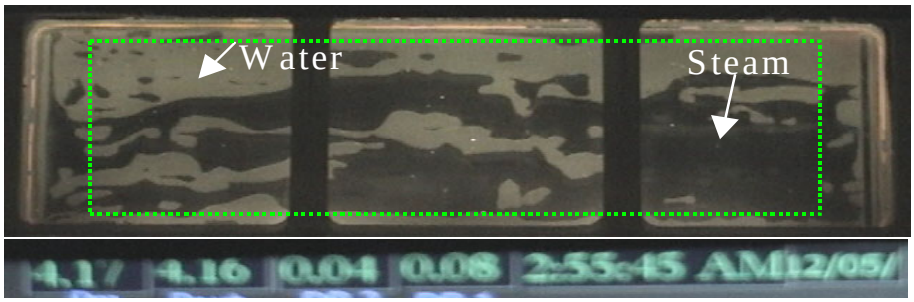

Figure 1.19: Sample video image taken for steam-water runs.

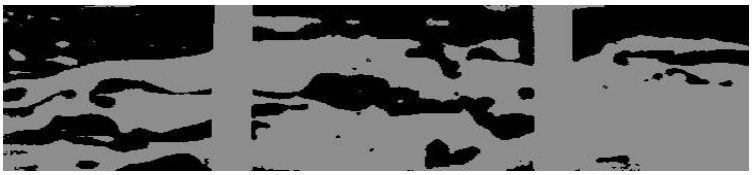

Figure 1.20: Processed gray scale image used in measuring saturation.

Pan et al. (1996) also used this technique for measurement of saturation. This study noted that the sources of error in this technique were the quality of the photographs and the water film adsorbed on the surfaces of the plates with the latter being of minimal effect. Good quality photographs are the ones with clear distinction between the gas and liquid phase. Good lighting is necessary so that the colors in the image come out clearly. The lighting should also be positioned in a way that it does not produce shadow on the flow area. The program will mistakenly take the shadow as steam phase even if there is liquid.

According to the nitrogen-water experiments by Diomampo (2001) and others, these fracture flow experiments are not expected to reach a perfect steady state. Instead, they are unsteady by nature. There are significant pressure fluctuations accompanied by saturation changes and the gas and liquid flow rates vary. Due to this behavior, the data acquisition task requires frequent gathering of instantaneous pressure, flow rate and saturation values. Instantaneous gathering of data was accomplished by the use of the digital video camcorder. Video shots were taken of the pressure, time and saturation data displayed all at the same time. Pressure and temperature data and related time were displayed by the LCD monitor connected to the computer, which also ran the data acquisition system. The

saturation was computed from the image of the whole flow area of the fracture. The methodology used to integrate all the data and signals and then calculate the steam-water relative permeabilities is illustrated in the flow chart in Figure 1.21.

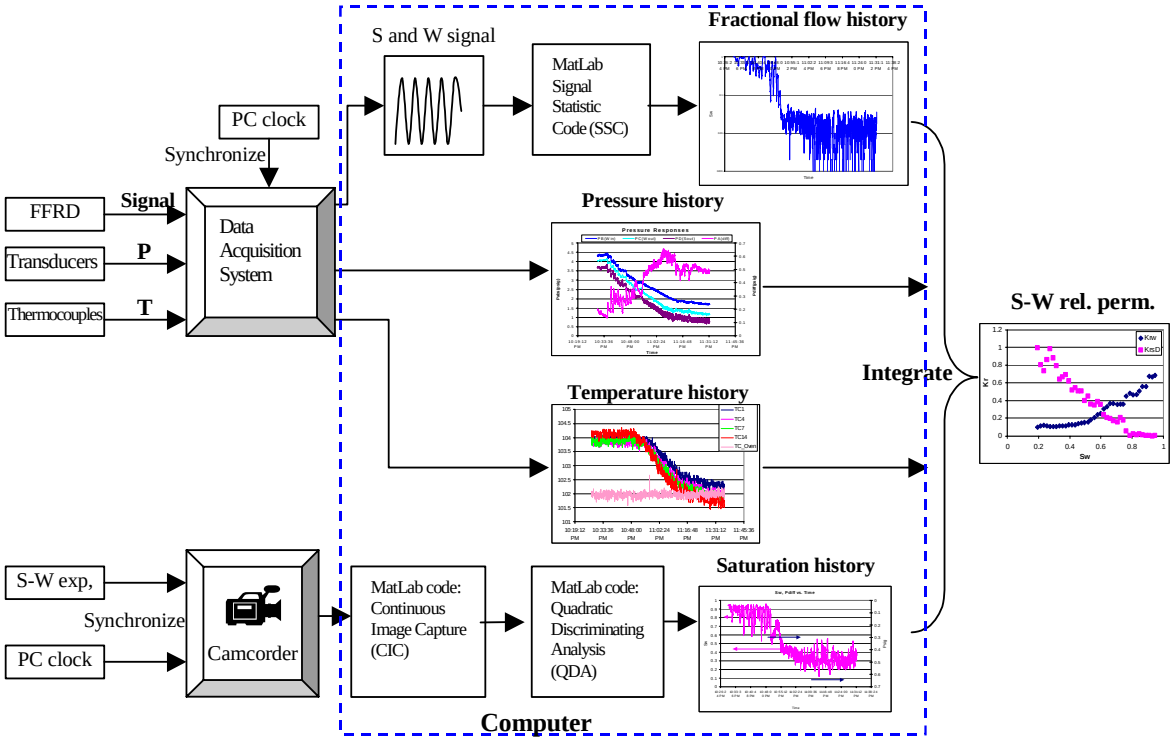

Figure 1.21: Data and signal processing flowchart.

1.5 EXPERIMENTAL RESULTS

Steady-state nitrogen-water experiment at room temperature (24 °C)

A steady-state nitrogen-water relative permeability experiment was conducted under a 24°C environment. Before the experiment, the absolute permeability of the smooth-walled fracture was measured. As can be seen in Figure 1.22, with the 0.013cm fracture aperture, the average permeability of the fracture measured is 1505 darcies when the back pressure is less than 2 psig. While applying the cubic law from Eq. 1.3, the permeability estimated is 1408 darcies. This is close to our measurement. Figure 1.23 illustrates one run of this steady-state experiment. Input rates of water and gas were 10 *ml/min* and 50 *ml/min* respectively. Clearly, unlike in porous media, even though constant gas and water rates were input to the fracture, the water saturation kept fluctuating in the fracture and the instantaneous f_w sensed from the FFRD followed this saturation fluctuation as shown in the top plot of Figure 1.23. The corresponding pressure response was also recorded as shown in the bottom plot of Figure 1.23. The gas-water flow in the fracture was unstable.

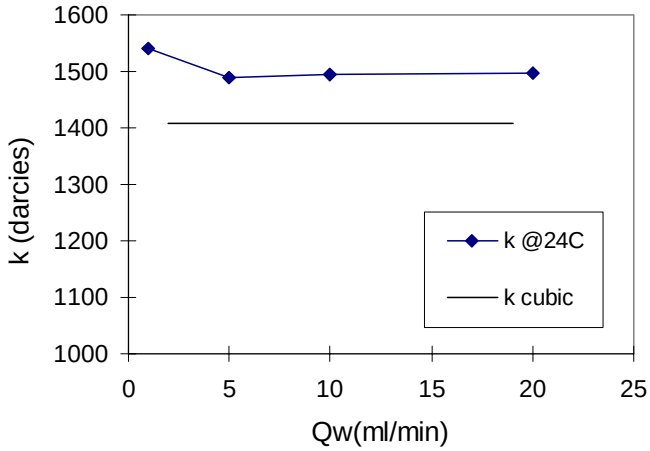

Figure 1.22: Absolute permeability of the fracture (aperture = 0.013cm) at 24°C with different liquid rates.

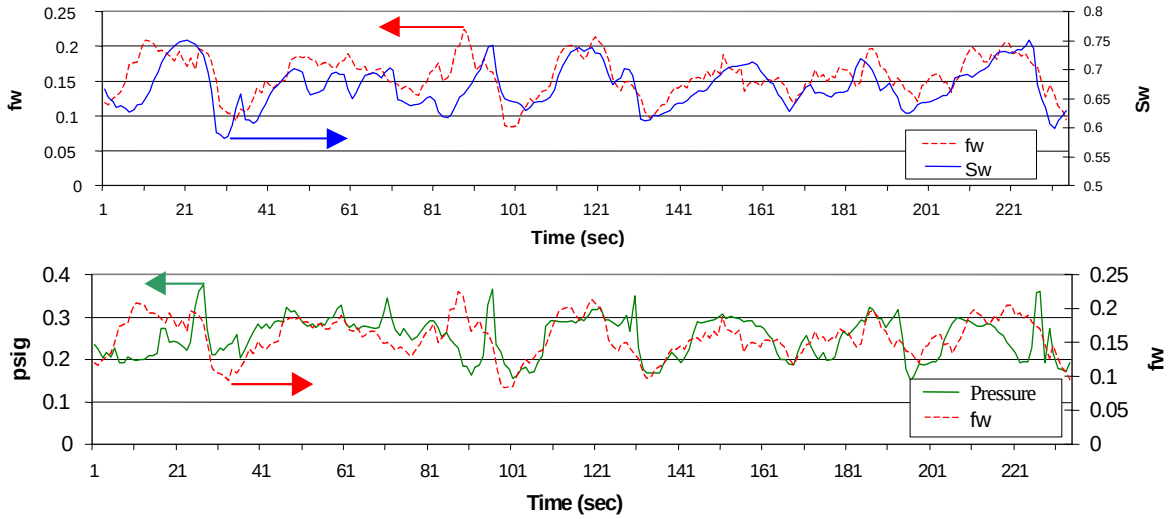

Figure 1.23: the relationship among water saturation, water fractional flow and pressure difference along the fracture at rates of Qw=10ml/min, Qg=50ml/min.

More than 3000 still images were extracted from the digital video and used for the flow pattern characterization and saturation calculation. Several types of flow patterns observed under high, intermediate, and low water saturation are shown in Figure 1.24, 1.25 and 1.26 respectively. Each figure shows four consecutive images. Figure 1.24 shows the nitrogen-water flow under high water saturation. Nitrogen moves in narrow slugs and flows discontinuously because of the relatively low gas flow rate. The higher pressure drop happens mostly when a slug tries to break through the water region (right images). Once the slug reaches the outlet of the fracture, the pressure drop decreases. This type of slug movement was seen frequently in high water saturation situations. Figure 1.25 shows the nitrogen-water flow at intermediate water saturation. Unlike the high water saturation case, the gas forms its own flow path through the fracture and gas and water behave nearly like layer flows under intermediate water saturation. Most of the gas flows in the upper region of the fracture, while most of the water flows in the lower. As can be seen in these four images, the gas flow path is stable. If a longer time scale is used to observe the behavior, some gas channels are seen to be blocked, and some are seen to be unblocked by water. In

other words, the gas flow path undergoes continuous snapping and reforming due to the invasion of water. These pictures were taken at a gas rate of 200 ml/min and water rate of 2 ml/min. Figure 1.26 shows the nitrogen-water flow under low water saturation. In this gas-dominated case, water flows through some narrow paths and sometimes as slow slugs as shown in the figure. The pressure drop along the fracture is fairly stable in this condition.

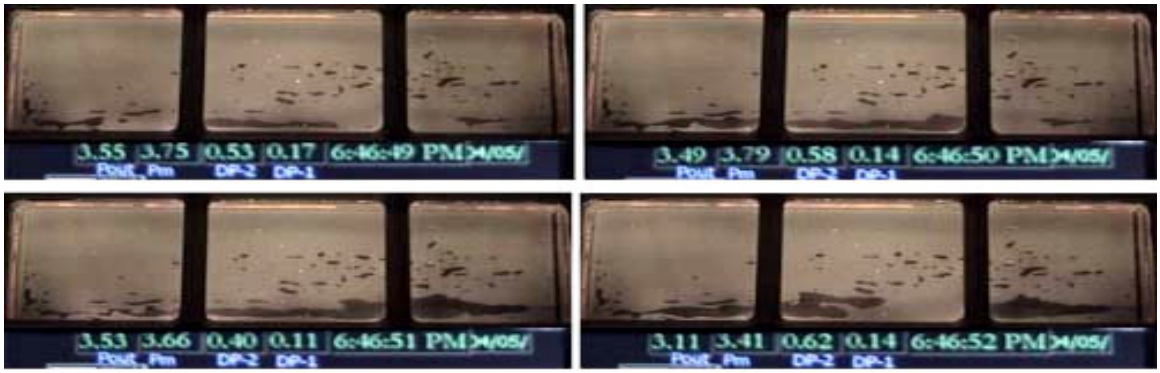

Figure 1.24: The continuous nitrogen-water flow behavior in smooth-walled fracture at room temperature under high water saturation (~90%) (nitrogen phase is dark, water phase is light, Qw=10ml/min, Qg=5ml/min).

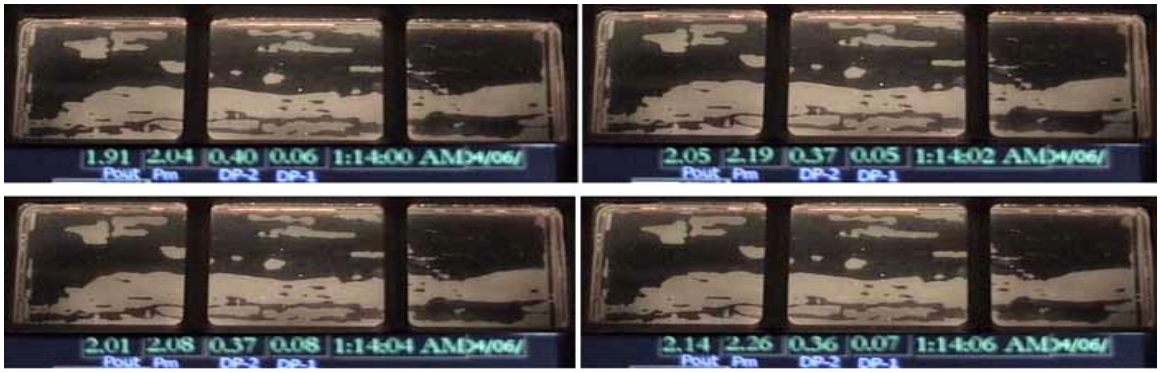

Figure 1.25: The continuous nitrogen-water flow behavior in smooth-walled fracture at room temperature under intermediate water saturation (~40%) (nitrogen phase is dark, water phase is light, Qw=2ml/min, Qg=200ml/min).

Figure 1.26: The continuous nitrogen-water flow behavior in smooth-walled fracture at room temperature under low water saturation (~15%) (nitrogen phase is dark, water phase is light, Qw=0.5ml/min, Qg=200ml/min).

Steady-state, nitrogen-water relative permeabilities at room temperature (24°C) over these more than 3000 data points were calculated and are shown in Figure 1.27. Window averages over the 2% saturation range from those comprehensive points are also shown in the same figure. Comprehensive water relative permeabilities are scattered under high water saturation owing to the slug flow in gas phase as shown in Figure 1.24. The vertical scattered effect in the gas relative permeabilities under extremely low water saturation may be associated with either the pressure fluctuation due to the slow moving water slugs as shown in Figure 1.26 or the difficulty in sensing the instantaneous f_w from the FFRD at low f_w. The average nitrogen-water relative permeabilities show good linearity in water values. Gas curves are more convex compared to the water values. Essentially, the average relative permeability curve shows less phase interference compared to the general relative permeability curves in porous media (Corey-type curves).

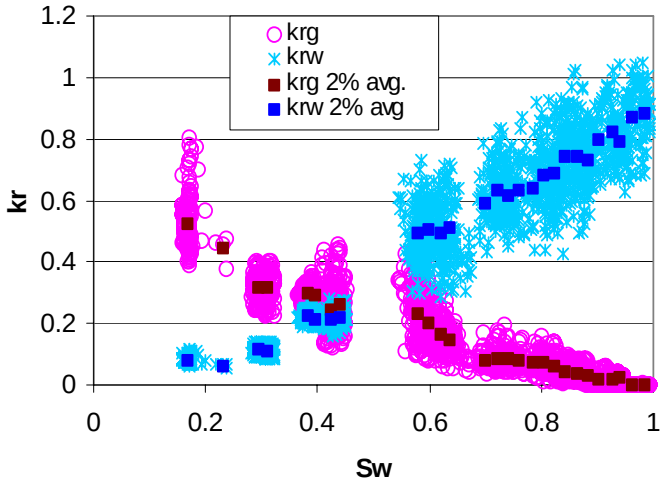

Figure 1.27: Comprehensive steady-state nitrogen-water relative permeabilities in the smooth-walled fracture at room temperature and their 2% window averages.

Steady-state nitrogen-water experiment at high temperature (90 °C)

The steady-state high-temperature nitrogen-water relative permeability experiment was conducted under a 90°C environment. Before the experiment, the absolute water permeability was measured. As shown in Figure 1.28, with 0.013 cm fracture aperture, the average permeability of the fracture measured is 1387 darcies which is slightly smaller than the permeability measured at 24°C (1505 darcies). Therefore the absolute permeability appears to decrease when the temperature increases. While using the cubic law from Eq. 1.3, the permeability estimated is 1402 darcies. This is close to our measurement.

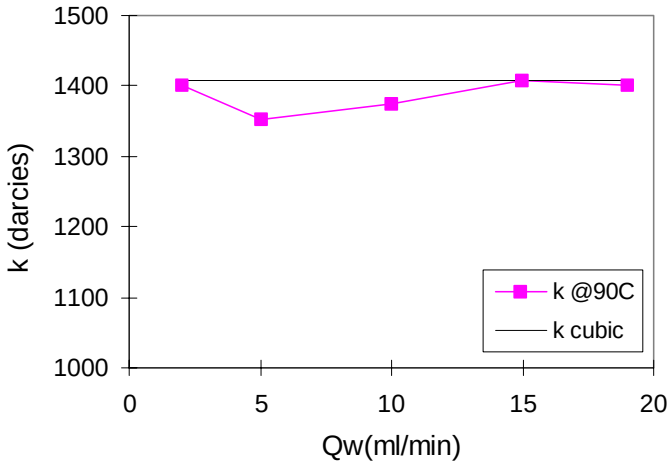

Figure 1.28: Absolute permeability of the fracture (aperture = 0.013cm) at 90^{o}C with different liquid rates.

As in the room temperature experiment, several types of flow patterns were observed under high, intermediate, and low water saturation as shown in Figures 1.29, 1.30 and 1.31 respectively. Each figure shows four consecutive images taken over either one or two second periods. Figure 1.29 shows the nitrogen-water flow under high water saturation. The flow regime under this condition is similar to that at room temperature (Figure 1.24). Nitrogen moves as narrow slugs and flows discontinuously because of the relatively low gas rate. Also more immobile gas is seen in Figure 1.29 in comparison to Figure 1.24.

Figure 1.30 shows the typical nitrogen-water flow behavior under intermediate water saturation. Similar to the room temperature case, the gas forms very stable flow paths through the fracture and the gas and water behave like layer flows. Almost all of the gas flows solely in the center region of the fracture, while most of the water flows above and below the gas path. Except for a small amount of immobile water inside the central gas channel, the gas path is more uniform and is not tortuous. These images were taken at a gas rate of 150 *ml/min* and water rate of 7.5 *ml/min*.

Figure 1.31 shows the nitrogen-water flow under low water saturation. Comparing Figure 1.31 to Figure 1.26, it is clear that the water saturation is much smaller than that in the room temperature case (Figure 1.26) when input rates are the same (Q_w=0.5*ml/min* and Q_g=200*ml/min* in both cases). The instantaneous f_w sensed was also smaller than that in room temperature case. Consequently, some water evaporated into the gas phase during the two-phase flow due to the high temperature and relatively large gas flow rate. It is necessary to evaluate the evaporation rate and the steam ratio in the gas phase since the gas phase contains not only nitrogen but also some amount of water vapor in this high-temperature case.

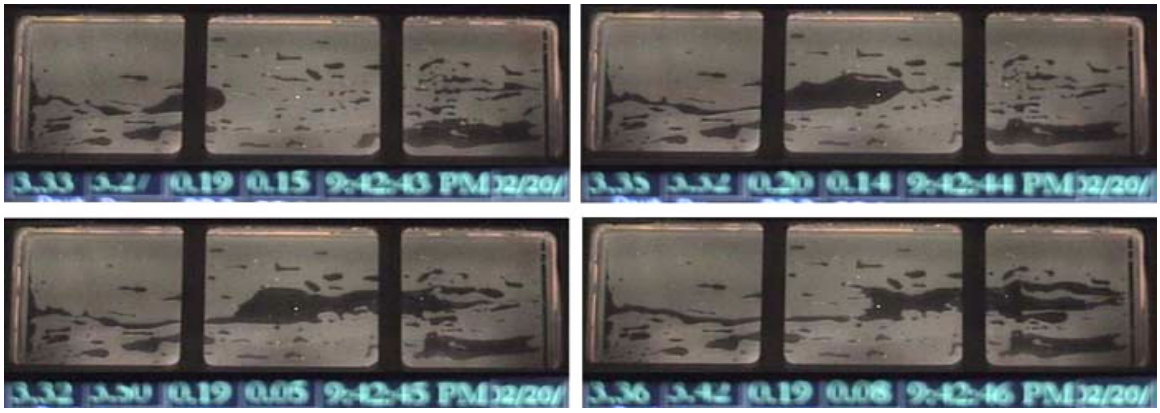

Figure 1.29: The continuous nitrogen-water flow behavior in smooth-walled fracture at high temperature (90^{o}C) under high water saturation (>80%) (nitrogen phase is dark, water phase is light, Qw=10ml/min, Qg=5ml/min).

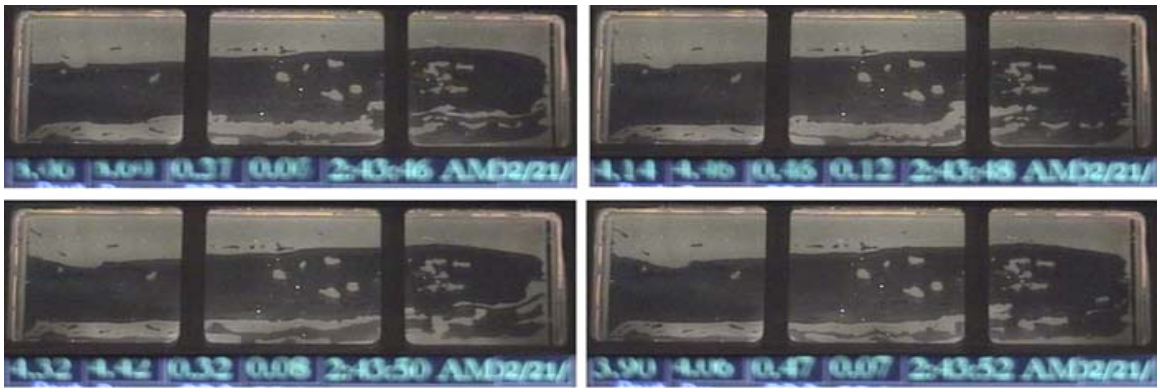

Figure 1.30: The continuous nitrogen-water flow behavior in smooth-walled fracture at high temperature (90^{o}C) under intermediate water saturation (~40%) (nitrogen phase is dark, water phase is light, Q_w=7.5ml/min, Q_g=150ml/min).

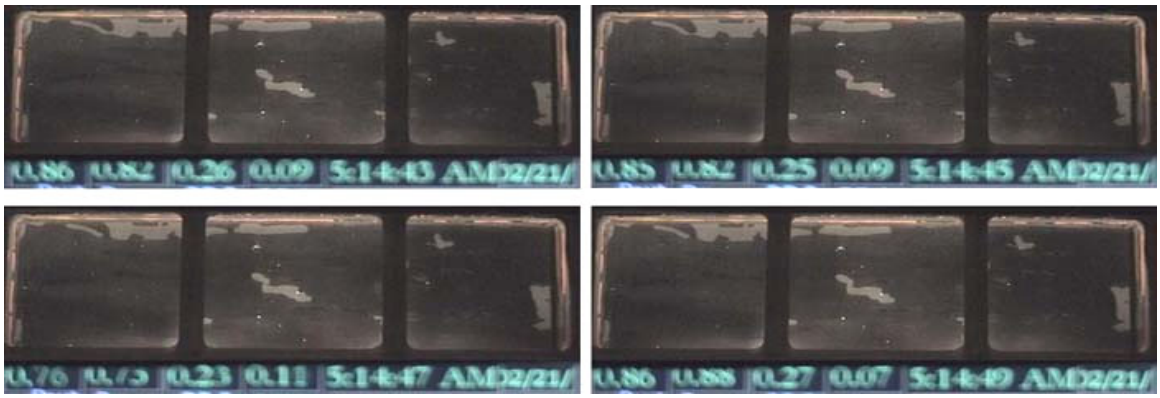

Figure 1.31: The continuous nitrogen-water flow behavior in smooth-walled fracture at high temperature (90^{o}C) under low water saturation (~5%) (nitrogen phase is dark, water phase is light, Q_w=0.5ml/min, Q_g=200ml/min).

It is worth noting that during the nitrogen-water experiment at 90^{o}C, there was a strong effect of evaporation from the water phase, which increases the volumetric flow rate of the gas. Therefore, there is not only pure nitrogen but also water vapor in the gas phase. The gas viscosity used in Eq. 1.6 has to be the mixture-gas viscosity instead of the pure

nitrogen viscosity. The viscosity of the mixture of nitrogen and water vapor can be expressed as:

$$\mu_{mix,g} = \frac{\mu_{N2,g} Q_{N2,g} + \mu_{w,g} Q_{w,g}}{Q_{N2,g} + Q_{w,g}} \tag{1.24}$$

where, $\mu_{N2,g}$ and $\mu_{w,g}$ are the nitrogen viscosity and water vapor viscosity respectively; $Q_{N2,g}$ and $Q_{w,g}$ are the nitrogen volumetric rates and water vapor volumetric rates which will be calculated from the water evaporation rate, X obtained from Eq. 1.25.

The water evaporation rate can be evaluated by using the FFRD measurements. Instantaneous f_w obtained from the FFRD can be used to calculate evaporation rate, X, given input water and gas (nitrogen) rates. By using the mass balance theory, X can be calculated by Eq. 1.25:

$$X = \frac{Q_{w0,l} - f_w (Q_{w0,l} + Q_{N2,g})}{1 + f_w (\frac{v_{w,g}}{v_{w,l}}) - f_w} \tag{1.25}$$

where, $Q_{w0,l}$ and $Q_{N2,g}$ are the input liquid water rate and gas rate respectively; $v_{w,l}$ and $v_{w,g}$ are the specific volume for water and steam (or water vapor) at some specific temperature; f_w is the instantaneous water fractional flow measured by the FFRD. The evaporation rate evaluated from Eq. 1.25 with different gas rates in this high-temperature experiment is presented in Figure 1.32. Generally, the evaporation rate increases while the gas rate increases. Figure 1.33 shows the gas fractional flow, f_g, versus the steam ratio which is the volume of the steam evaporated from the water phase to the total volume of gas (sum of the input gas and produced steam). Most of steam ratios stay below 0.5 as f_g is less than 0.97. In extremely high f_g situations, i.e. gas rates are much larger than water rates, steam ratios increase gradually and reach a maximum value of 0.7.

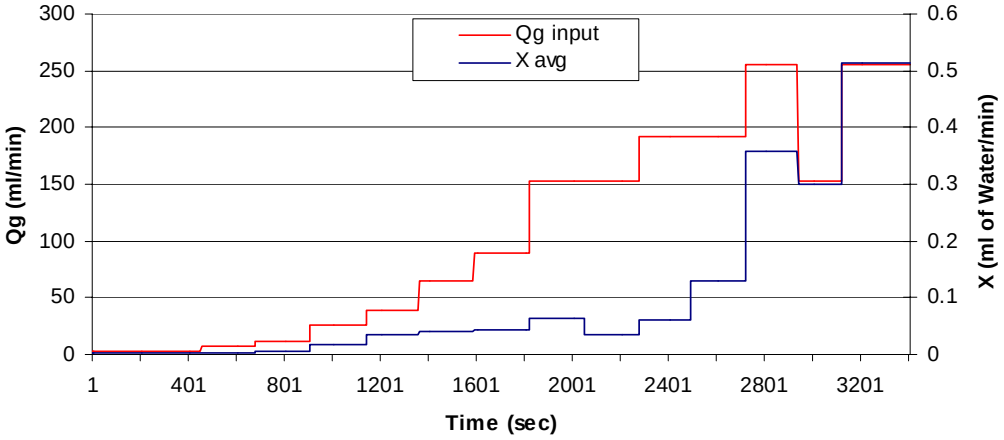

Figure 1.32: Water evaporation rates versus gas rates in the steady-state nitrogen-water experiment at 90^{o}C.

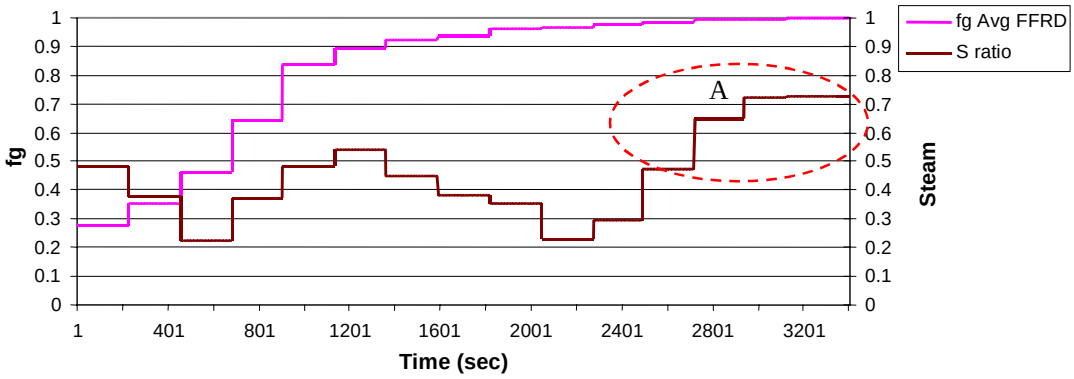

Figure 1.33: Steam ratios versus gas fraction flow in the steady-state nitrogen-water experiment at 90°C.

Comprehensive high-temperature nitrogen-water relative permeabilities obtained from over 3000 points are shown in Figure 1.34. The 2% window averages are also provided in the same figure. Generally, high-temperature nitrogen-water relative permeability values behave similar to the room temperature case (Figure 1.27) with the exception of low water saturation cases where the gas-phase relative permeabilities in the high temperature case are much greater then those at room temperature.

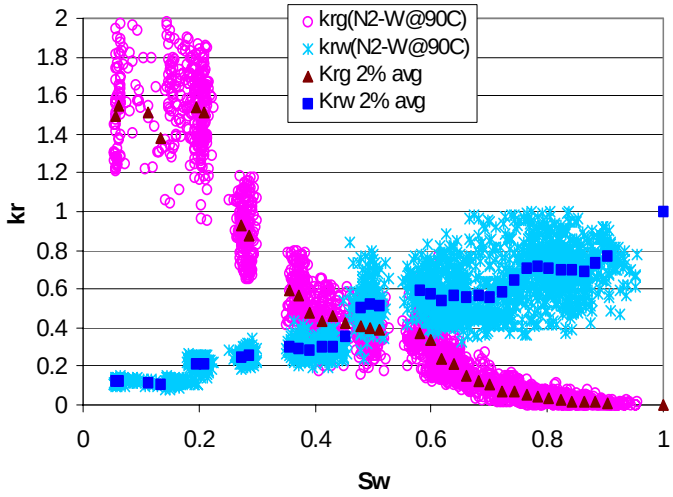

Figure 1.34: Comprehensive steady-state nitrogen-water relative permeabilities in the smooth-walled fracture at high temperature (90°C) and their 2% window averages.

Steam-water experiment

Unsteady and steady-state steam-water relative permeability experiments were conducted at around 104°C. The procedure and detail of the unsteady steam-water relative permeability experiment were described in Chen et al. (2002). The procedure of the steady-state experiment is similar to the unsteady experiment, except data were obtained when the steam-water flow reached steady state, or underwent repeatable flow regime changes even though the flow was unstable. The flow regime under high water saturation conditions behaved similarly to the nitrogen-water case. As can be seen in Figure 1.35, the steam phase flows in fast moving slugs. The shape of slugs is more amorphous than that in the

nitrogen-water case. The steam-water flow behavior is different from that of the nitrogen-water case under intermediate and low water saturations. As illustrated in Figures 1.36 and 1.37, the steam can flow via slugs, bubbles, and channels. On the other hand, the water flows via water slugs, water bubbles, and water channels. Even under the low water saturation conditions, the steam-water flow is still unstable. The steam phase and water phase can flow together in several different forms. This two-phase cocurrent flow situation was rarely seen in the nitrogen-water case.

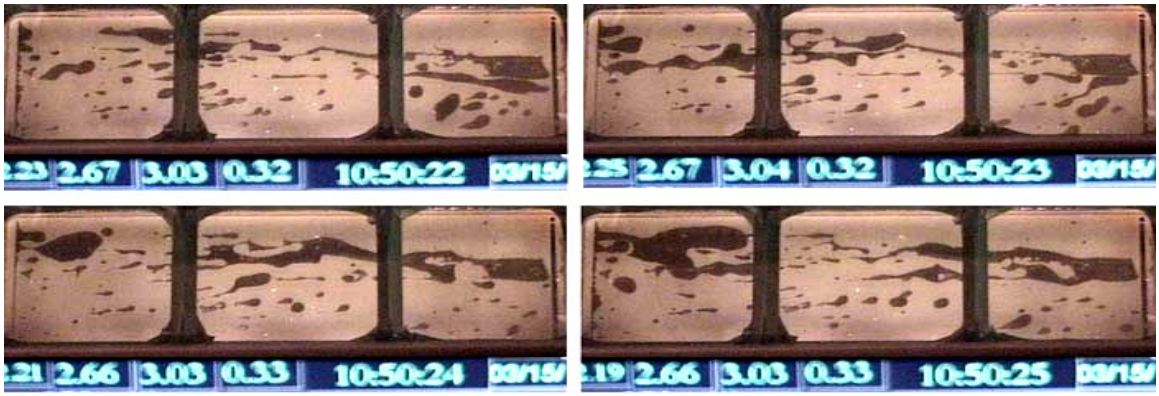

Figure 1.35: The continuous steam-water flow behavior in smooth-walled fracture under high water saturation (~90%). (steam phase is dark, water phase is light).

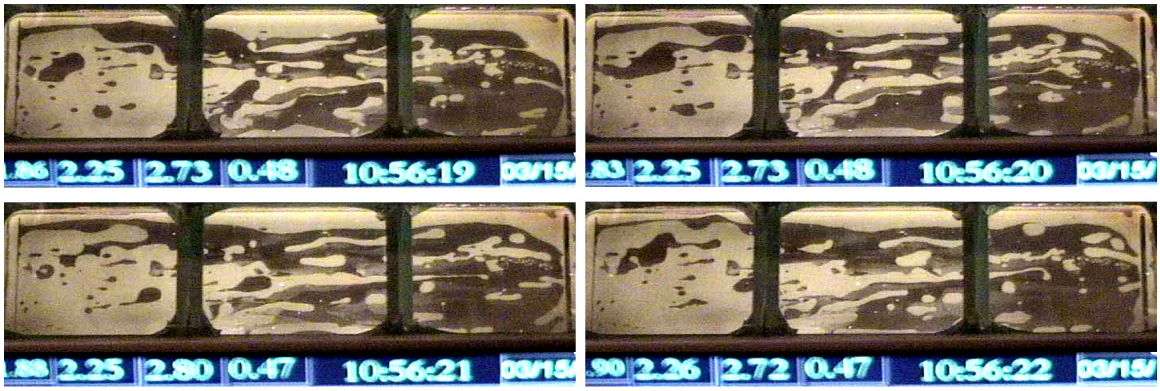

Figure 1.36: The continuous steam-water flow behavior in smooth-walled fracture under intermediate water saturation (~40%).

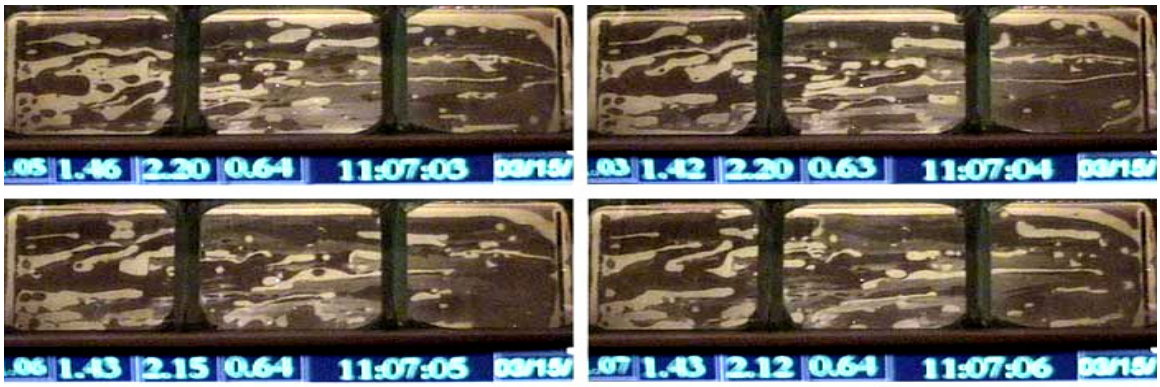

Figure 1.37: The continuous steam-water flow behavior in smooth-walled fracture under low water saturation (~20%).

Figure 1.38(a) and (b) show comprehensive steam-water relative permeability values from both unsteady and steady experiments. The k_{rw} values behave smoothly in both cases, whereas the k_{rs} values are more scattered in the unsteady case. This may be because the error and uncertainty increase when steam-water flow is in unsteady condition. The major errors in the unsteady experiments are the delay of f_s and f_w measurement from the FFRD, the FFRD detection limit, and the pressure fluctuation in the unstable high-temperature fracture flow. The steady-state experiment was conducted after improving the FFRD detection limit and pressure fluctuation problems; therefore, a less scattered result was expected in the steady experiment. Comparing Figure 1.38 to Figure 1.27 and 1.34, comprehensive steam-water relative permeabilities are more scattered than nitrogen-water cases in general. Nevertheless all of these four results (nitrogen-water at 24°C, nitrogen-water at 90°C, unsteady steam-water, steady steam-water experiments) are all scattered to varying degrees. This scattered effect can be associated with the fluctuating and unstable nature of the multiphase flow in fractures.

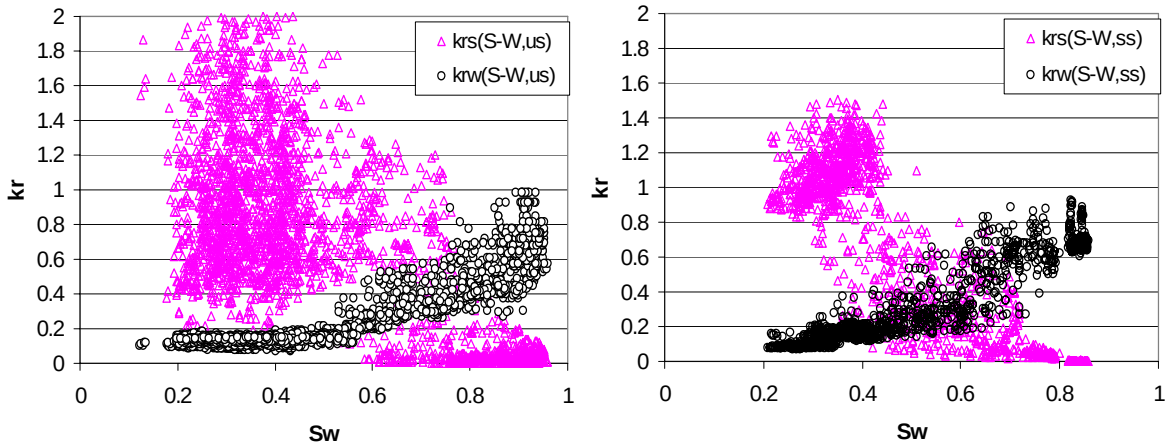

(a) (b)

Figure 1.38: Comprehensive steam-water relative permeabilities in both unsteady (a) and steady-state (b) experiments.

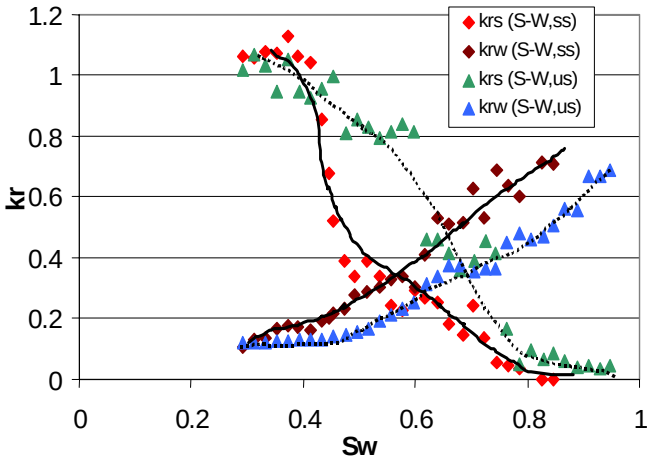

Figure 1.39: Steam-water relative permeabilities in both unsteady and steady-state experiments by applying 2% S_w averages.

Averages of the relative permeabilities over 2% saturation ranges from Figure 1.38(a) and (b) are shown in Figure 1.39, while the lines in Figure 1.39 are to facilitate the comparison only. The figure shows good correlation in both steam and water curves. End points of these two experiments are close; however, the gas curve in the unsteady experiment shows less convexity than that in the steady case, while the water curve in the unsteady experiment is slightly lower than in the steady case. These differences in the unsteady results can be attributed to the measurement errors due to the unsteady experimental conditions and the technical problems in the FFRD as mentioned before. Steam-water relative permeability curves show less phase interference and are not close to the Corey-type relative permeability behavior.

1.6 DISCUSSION

Comprehensive nitrogen-water relative permeabilities at room (24^oC) and high temperature (90^oC) are shown in Figure 1.40. Data points from room temperature and high temperature cases show acceptable correlation. In both cases, comprehensive water relative permeabilities are scattered under high water saturation owing to the slug flow in the gas phase as shown in Figure 1.29. The vertical scattered effect in the gas relative permeabilities under extremely low water saturation may be associated with either the pressure fluctuation due to the slow moving water slugs as shown in Figure 1.31 or the difficulty in sensing the instantaneous f_w from the FFRD at low f_w. Overall, nitrogen-water relative permeability values at 90^oC are greater than those at 24^oC.

Figure 1.41 shows moving window averages of the full results shown in Figure 1.40. The trend lines in Figure 1.41 are to facilitate the comparison only. The water-phase relative permeability values at these two different temperatures are close and behave almost the same as the water line of the X-curve (linear line with slope=1). The gas-phase relative permeability values at these two different temperatures show different behaviors. It is evident that the gas curve at 90^oC is higher than that at 24^oC. In Figure 1.41, when water saturation is less than 0.5, the gas-phase relative permeability values at 90^oC show a more significant increasing trend in comparison to the case of 24^oC. This difference may be attributed to the increase of the steam ratio because of the strong evaporation effect at 90^oC as shown in Figure 1.33. In the high-temperature, nitrogen-water experiment, water can evaporate to the vapor phase, especially in a high gas rate situation. As shown in part A in Figure 1.33, when gas fractional flow, f_g, is close to 1, the steam ratio reaches 0.73. This corresponds to part A in Figure 1.41. This may indicate that the more water vapor in the gas phase, the higher the gas-phase relative permeability values. However, it might be questionable that the gas-phase relative permeability values near the end point are more than unity in the 90^oC case. This overestimated behavior can be attributed to both the unstable thermodynamic properties due to the evaporation effect and the overestimation of gas flow rates measured from the outlet of the fracture.

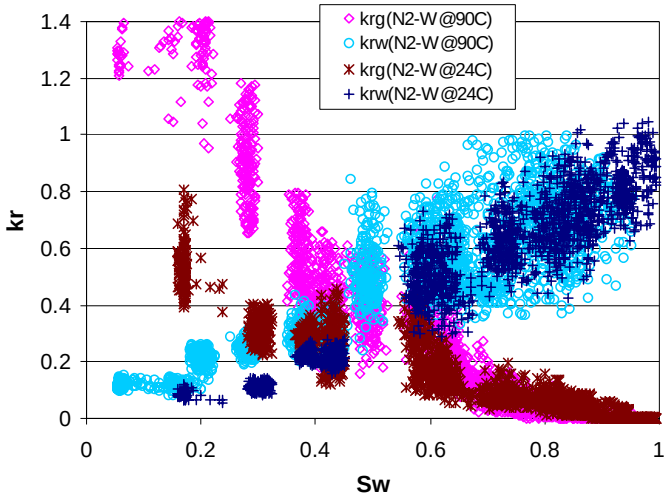

Figure 1.40: Comparison of comprehensive nitrogen-water relative permeabilities between 90°C and 24°C in the smooth-walled fracture.

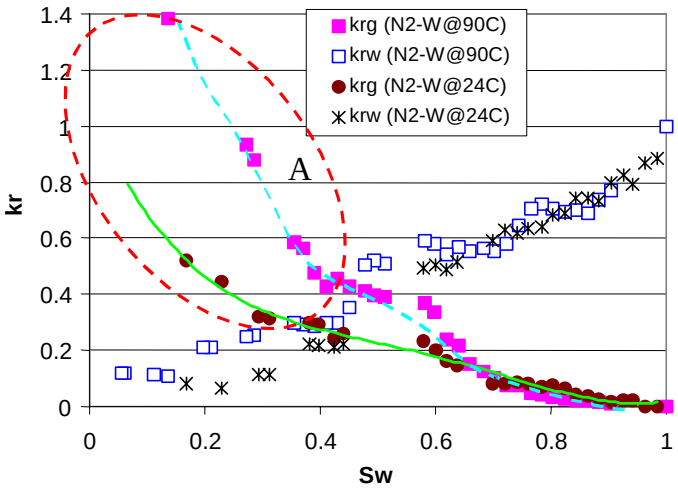

Figure 1.41: Comparison of average nitrogen-water relative permeabilities between 90°C and 24°C in the smooth-walled fracture.

Figure 1.42 compares window averages of relative permeabilities between steady steam- and nitrogen-water cases in the smooth-walled fracture. Liquid curves have almost identical trends except at low water saturation ranges where the steam-water case may lose some accuracy because of the detection limit of the FFRD. On the other hand, the gas curves behave very differently. The steam curve shows a much more mobile character than the nitrogen curve, which can be seen from the higher relative permeability values in the steam curve in Figure 1.42. This phenomenon was also observed from the digital images. The nitrogen curve at 90°C is higher than that at 24°C. This shows the consistency with some theoretical research and some experimental measurements in porous media. In spite of this, the nitrogen-water experiment at 90°C and the steam-water experiment might overestimate the gas-phase relative permeabilities because of the overestimation of the gas rates as described before. The gas flow rates correction by using image processing approaches is in progress.

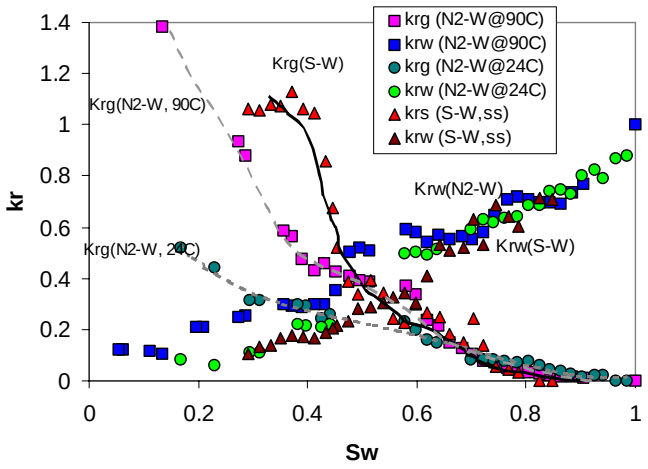

Figure 1.42: Comparison of relative permeability curves between steam- and nitrogen-water cases in the smooth-walled fracture.

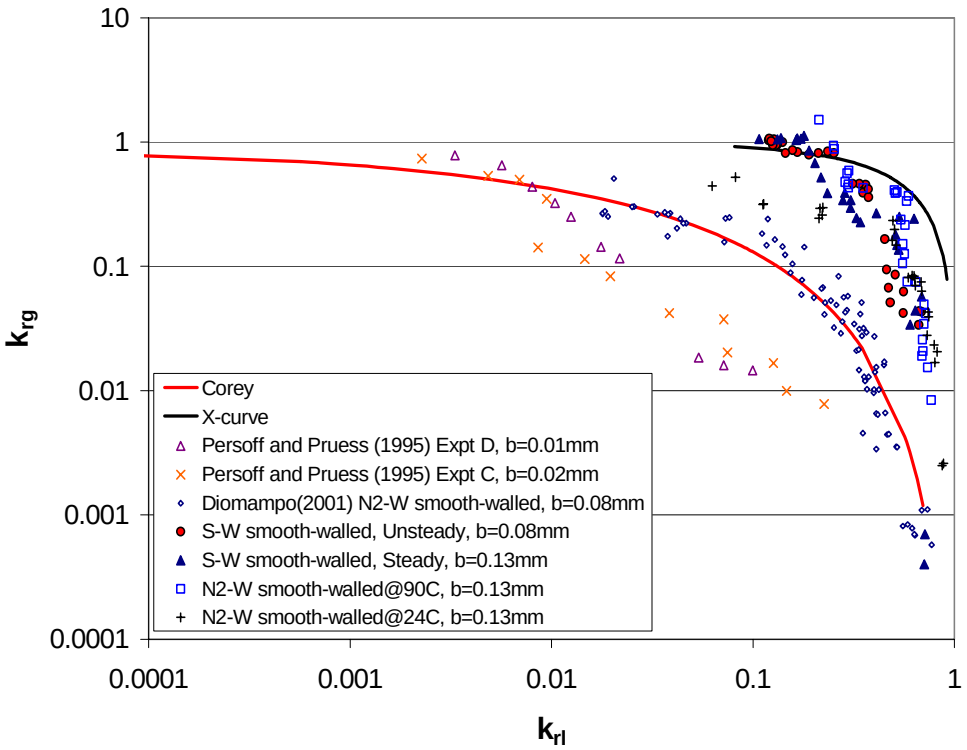

Figure 1.43: Comparison of steam- and nitrogen-water relative permeabilities in this research with previous measurements of air-water relative permeabilities in fractures.

Figure 1.43 summarizes the recent measurements of gas-water relative permeabilities in fractures in comparison to a collection of previously published results. Comparing the current results with previous measurements of air-water relative permeabilities in fractures, both steam- and nitrogen-water values from this research behave close to X-curve, which represents a behavior different from previous published measurements. Most of the previously published results proposed that air-water relative permeabilities in fractures follow the Corey-type curve or lie below it. It is necessary to mention that some of

fractures in these studies were rough-walled. Currently, the roughness of the fracture has not yet been considered in this research. Furthermore, the apertures of the fractures may play an important role in the shape of the relative permeability curves. Capillary forces become more and more significant as apertures decrease. This might lead the relative permeabilities to behave more like the Corey curves as can be seen in Figure 1.43. On the other hand, viscous forces dominate as apertures increase. This leads the relative permeabilities to behave closer to the X-curve. Romm (1966) also found similar X-curve behavior in his experiment with kerosene and water through an artificial smooth parallel-plate fracture lined with strips of polyethylene or waxed paper.

1.7 CONCLUSION

1. The steam-water flow behavior in fractures is different from that of nitrogen-water flow. This is particularly obvious in low water saturation conditions. The steam and water can flow concurrently in the smooth-walled fracture; contrarily, nitrogen and water have the tendency to block each other.
2. Steam-water relative permeabilities are different from nitrogen-water relative permeabilities in the smooth-walled fracture. Steam-phase curves show less phase interference in comparison to the nitrogen-phase curves while the water-phase curves are relatively similar.
3. Comparing with previous research into air-water relative permeabilities in fractures, both average steam- and nitrogen-water relative permeabilities behave closer to the X-curve in this research, which is similar to the result from Romm (1966) but is in contradiction to other recently published measurements.
4. An apparent temperature effect on nitrogen-water relative permeabilities is evident in the gas-phase curves. The higher gas-phase curve at 90^{o}C is due to both the effect of the evaporated steam and the overestimation of gas flow rates measured from the outlet of the fracture.
5. Comprehensive relative permeability plots show more scatter in the steam-water experiments. Furthermore, the steam-water flow seldom forms stable paths as observed from the digital images and videos. This indicates the unsteady nature of steam-water flow in fractures.

2. FRACTAL CHARACTERIZATION OF CAPILLARY PRESSURE IN THE GEYSERS ROCK

This research project is being conducted by Senior Research Engineer Kewen Li and Professor Roland Horne. The objective of this project is to characterize the heterogeneity of The Geysers rock using a fractal technique as a way of describing capillary pressure.

2.1 SUMMARY

Fractures play an important role in steam production from geothermal reservoirs. It has been a challenge to characterize materials with a high density of fractures such as rock from The Geysers. Experimental data showed that the capillary pressure curves of The Geysers rock are very different from that of Berea sandstone. Methods to characterize the difference between the two have been few. It was also found that the frequently-used Brooks-Corey model could not be used to represent the capillary pressure curves of The Geysers rock samples studied. To this end, a fractal technique was proposed to model the features of the capillary pressure curves and to characterize the difference between The Geysers rock and Berea sandstone. The calculated values of the fractal dimension of all the core samples studied (six from The Geysers and one Berea sandstone) were in the range from 2 to 3. The results demonstrated that The Geysers rock with a high density of fractures had a greater fractal dimension than Berea sandstone that is almost without fractures. This shows that The Geysers rock has greater heterogeneity, as expected. The significance of fractal dimension inferred from capillary pressure data is consistent with the traditional qualitative observation from the frequency graph of pore size distribution. The proposed fractal technique may be extended from core scales to reservoir scales to characterize fracture density in geothermal reservoirs.

2.2 INTRODUCTION

Reserves of geothermal reservoirs depend mainly on the porosity of the rock matrix while steam and water production rates primarily depend on fractures. It is relatively easy to measure the values of porosity in the rock matrix. On the other hand, it is difficult to measure or characterize the fracture systems quantitatively as well as the entire rock with both matrix and fractures. Recently attention has been paid to the fractal characterization of the fracture surface (Babadagli and Develi, 2000) and the space distribution of fractures in geothermal reservoirs (Sammis *et al.*, 1992; Tateno *et al.*, 1995; Tsuchiya and Nakatsuka, 1995).

Tateno *et al*. (1995) demonstrated that the distribution of open fracture width in a geothermal reservoir was fractal. Sammis *et al*. (1992) studied the fracture pattern and the distribution of fractures in two dimensions at The Geysers geothermal field. Sammis *et al*. (1992) found that the values of the fractal dimension measured at different scales, the outcrop, roadcut, and regional scales, were almost the same.

However publications on the characterization of the entire rock with both matrix and fractures have been few. Studies on the features of capillary pressure curves of The Geysers rock and the corresponding pore size distribution have also been few. In this

study, the capillary pressure curves of The Geysers rock were measured using a mercury-injection technique. A fractal approach was proposed to characterize the rock heterogeneity quantitatively using the data from the capillary pressure curves. The values of the fractal dimension inferred from capillary pressure curves were used to represent rock heterogeneity as well as the differences between The Geysers rock and the more uniform, unfractured Berea sandstone.

2.3 THEORY

There have been many methods to characterize heterogeneity in nature. Of all the approaches, fractal geometry has been utilized widely in many areas. Fractal geometry is a branch of mathematics and is used mainly to characterize disordered or heterogeneous systems that appear similar in some way when observed at different scales. This feature is known as self-similarity or scale invariance. The Geysers rock is highly heterogeneous and extremely disordered and may be fractal in nature. In this study, we chose fractal geometry as a tool to characterize the heterogeneity of The Geysers rock with both matrix and fractures.

According to the basic concept of fractal geometry, the following expression applies to a fractal object:

$$N(r) \propto r^{-D_f} \tag{2.1}$$

where r is the radius (or characteristic length) of a unit chosen to fill the fractal object, $N(r)$ is the number of the units (with a radius of r) required to fill the entire fractal object, and D_f is the so-called fractal dimension. The fractal dimension is a representation of the heterogeneity of the fractal object. The greater the fractal dimension, the more heterogeneous the fractal object.

Capillary pressure curves measured by a mercury-injection technique are often used to infer the pore size distribution of rock samples. In making this inference, rock with solid skeleton and pores is represented by using a capillary tube model. $N(r)$ can be calculated easily once mercury-injection capillary pressure curves are available. The unit chosen in this study was a cylindrical capillary tube with a radius of r and a length of l. So the volume of the unit is equal to $\pi r^2 l$ and $N(r)$ at a given radius of r is then calculated easily.

Once $N(r)$ is known, the value of fractal dimension, D_f, can be determined from the relationship between $N(r)$ and r. The relationship between $N(r)$ and r should be linear on a log-log plot if the pore system of the rock is fractal.

2.4 EXPERIMENTAL MEASUREMENTS

Six core samples from different wells at The Geysers geothermal field were used in this study. Unfortunately the core samples were irregular and too small to drill a plug for permeability measurements. The measured porosity of the core samples ranged from 0.1 to 4.0%. One core sample of Berea sandstone was also used as a comparison. The porosity of the Berea sample was about 23.0% and the air permeability was about 804 md.

The surface tension of air/mercury is 480 mN/m and the contact angle through the mercury phase is 140^o (Purcell, 1949).

2.5 RESULTS

Capillary pressure curves of the six core samples from The Geysers geothermal field and one core sample of Berea sandstone were measured using the mercury-injection technique. The results are shown in Fig. 2.1. There are substantial differences between The Geysers rock and Berea sandstone. The normalized wetting-phase saturation is calculated as follows:

$$S_w^* = \frac{S_w - S_{wr}}{1 - S_{wr}} \tag{2.2}$$

where S_w^* is the normalized wetting-phase saturation (the wetting-phase in this study is air), S_w is the wetting-phase saturation, and S_{wr} is the residual saturation of the wetting-phase.

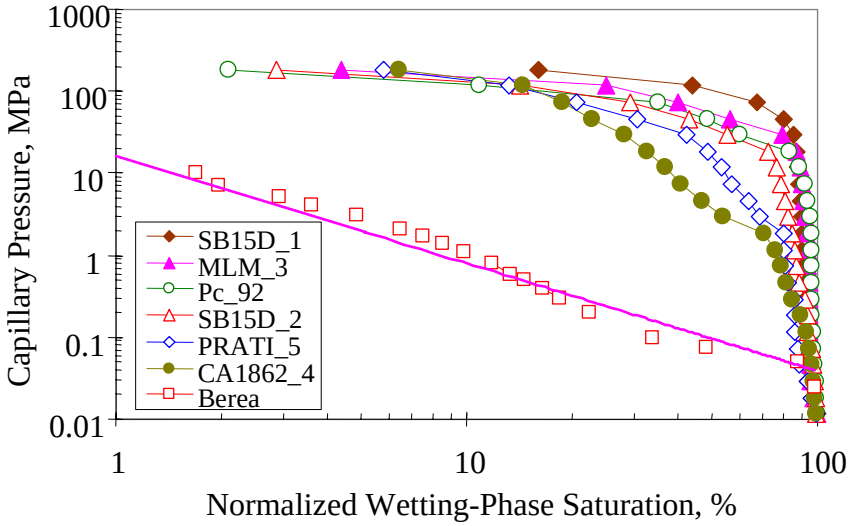

Figure 2-1: Capillary pressure curves of The Geysers rock and Berea sandstone.

The capillary pressure curve of the Berea sandstone core sample is linear on a log-log plot, which implies that the capillary pressure curve can be represented using the frequently-used Brooks-Corey model (1964). However all the capillary pressure curves of The Geysers rock samples are nonlinear, which implies that the capillary pressure curves may not be represented using the Brooks-Corey model. Qualitatively one can see that The Geysers rock samples are more heterogeneous than Berea sandstone, as expected.

The pore size (pore throat radius) distributions inferred from capillary pressure measurements are shown in Fig. 2.2. Note that the capillary tube model was used as usual. Fig. 2.2 shows that the pore sizes in The Geysers rock are much smaller than in the Berea sandstone.

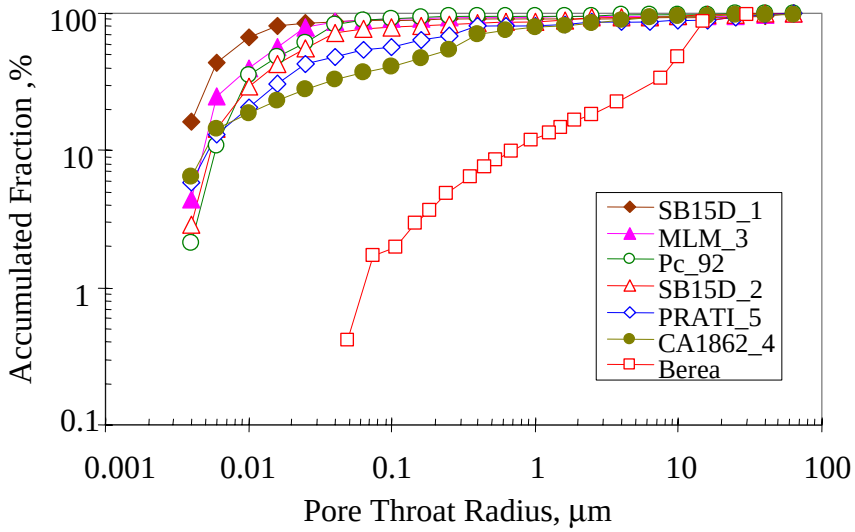

Figure 2.2: Pore size distributions of The Geysers rock and Berea sandstone.

To characterize the difference in heterogeneity between The Geysers rock and Berea sandstone, the capillary pressure curves shown in Fig. 2.1 were transferred to relationships between $N(r)$ and r according to Eq. 2.1. The results are shown in Fig. 2.3. We can see that all the curves of $N(r)$ vs. r are linear on a log-log plot, which implies that the pore systems of The Geysers rock and Berea sandstone are both fractal and can be characterized using the theories of fractal geometry. Note that about three data points in the beginning of mercury intrusion were off the main trend and were removed to conduct the regression analysis.

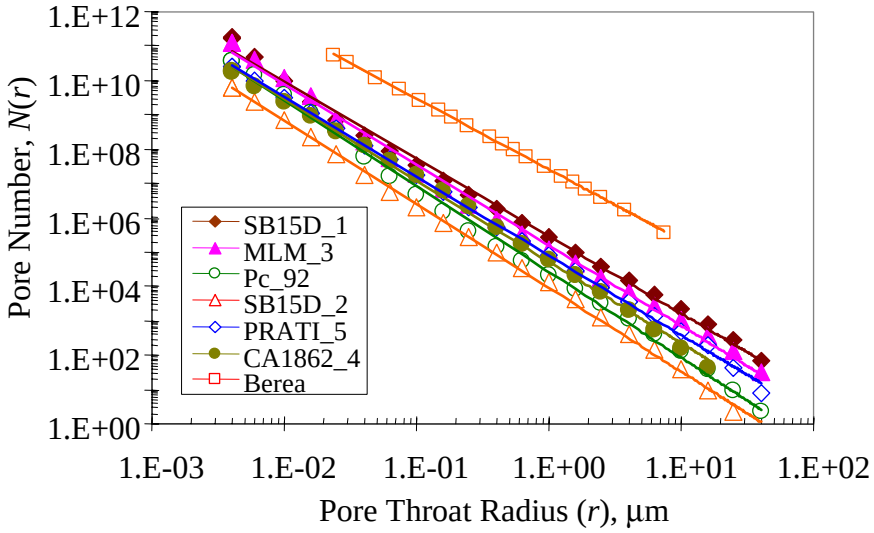

Figure 2.3: Relationships between $N(r)$ and r of The Geysers rock and Berea sandstone.

One can see from Fig. 2.1 that both Berea and The Geysers rock are fractal. However the values of the fractal dimension are different and can be used to characterize the differences between the two different rocks.

The values of the fractal dimension were calculated according to Eq. 2.1 for all the core samples using the data shown in Fig. 2.3 and the results are listed in Table 2.1.

Table 2.1: Fractal Dimensions of The Geysers rock and Berea sandstone.

Sample	SB15D_1	MLM_3	Pc_92	SB15D_2	PRATI_5	CA1862_4	Berea
ϕ (%)	4.0	2.5	0.4	0.1	1.1	0.8	23.0
D_f	2.2510	2.3407	2.4983	2.4356	2.3070	2.3645	2.0582

Table 2.1 shows that all the values of fractal dimension range from 2 to 3. The fractal dimension of Berea sandstone is much smaller than that of all the rock samples from The Geysers geothermal field. This observation implies that The Geysers rock is more heterogeneous than Berea sandstone, which is obviously true.

Rock heterogeneity can also be observed qualitatively from the frequency graph of pore size distribution. Figs. 2.4 and 2.5 show the pore size distributions of Berea sandstone and The Geysers rock (PRATI_5) respectively.

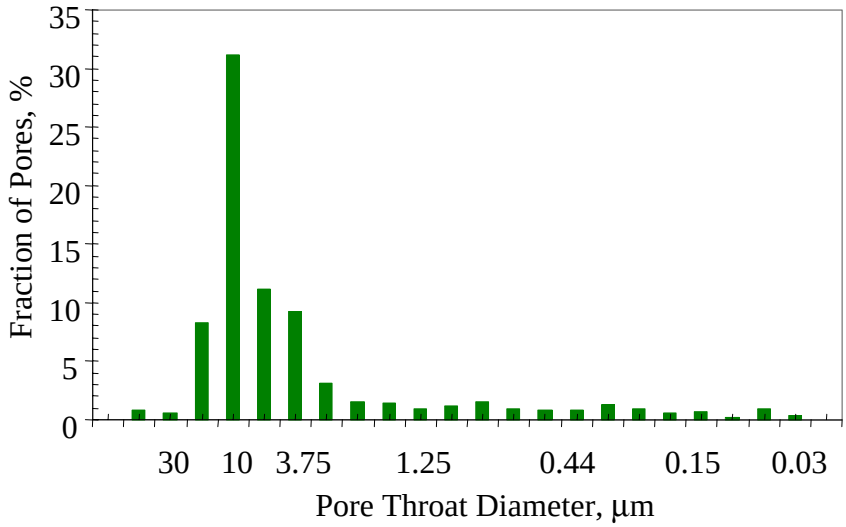

Figure 2.4: Pore size distribution of Berea sandstone.

The fraction of pores (vertical axis in Figs. 2.4 and 2.5) was calculated with the volume of injected mercury divided by the pore volume of the core sample. One can see that the pore size distribution of Berea sandstone is a normal distribution with a relatively narrow peak. However the pore size distribution of The Geysers rock (PRATI_5) is not a normal distribution and has many peaks. Comparing Fig. 2.4 to Fig. 2.5, it is obvious that The

Geysers rock (PRATI_5) has greater heterogeneity than Berea sandstone. This qualitative observation is verified by the values of fractal dimension inferred from capillary pressure curves (see Table 2.1).

The previous description also demonstrates that the significance of fractal dimension determined using Eq. 2.1 from capillary pressure data is consistent with the traditional qualitative observation from the frequency graph of pore size distribution.

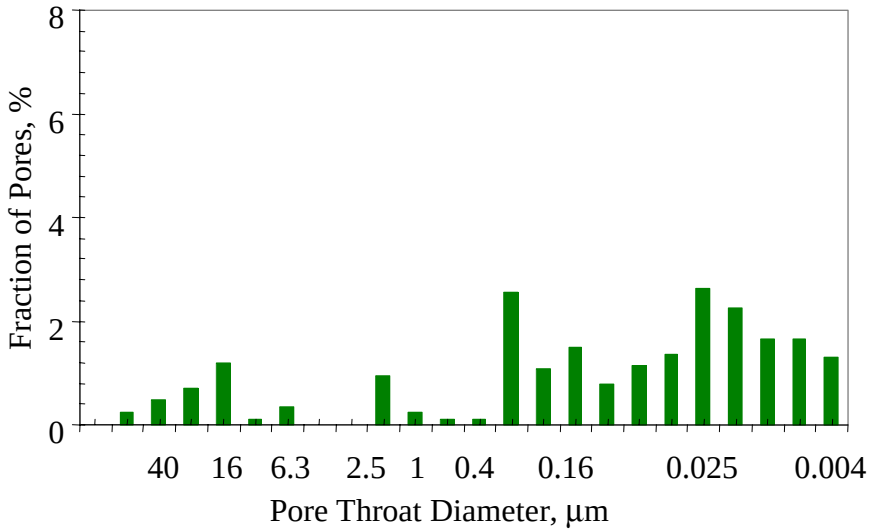

Figure 2.5: Pore size distribution of The Geysers rock (PRATI_5).

The results discussed in this section demonstrated that the fractal approach can be used to characterize the heterogeneity of The Geysers rock satisfactorily

2.6 DISCUSSION

In the petroleum industry, heterogeneity is a significant problem for oil production. Usually oil recovery in water drive reservoirs decreases with increase in heterogeneity. However this may not be the case in geothermal industry. Fractures are beneficial to the production of steam and water. Steam production rate may increase with fracture density. The greater fracture density implies greater heterogeneity, which can be characterized using fractal dimension. It would be helpful for reservoir engineers if a relationship between fractal dimension and steam production from geothermal reservoirs.

For water injection into geothermal reservoirs, the injection rate should not be greater than a specific value and should be optimized as pointed out by Li and Horne (2000). In this case, the injected water will not break through quickly at production wells and the fractures are beneficial. However the fractures may not be beneficial if the water injection rate is very high and greater than a critical value.

Shen and Li (1994, 1995) found a relationship between the fractal dimension of core samples and the oil recovery by water flooding. The core samples with greater values of fractal dimension had smaller values of water drive oil recovery. The experimental

observation is theoretically reasonable. This is because fractal dimension is a representation of rock heterogeneity. The greater fractal dimension implies greater heterogeneity. It is known that the oil recovery by water flooding is inversely proportional to the heterogeneity.

The relationship between the fractal dimension and the oil recovery by water flooding observed in laboratory was even true for oil recovery in many reservoirs developed by water injection, as reported by Shen and Li (1995). This is also understandable according to the features of fractal objects. Self-similarity is an important feature of a fractal. This feature implies that fractal dimension at the core scale may be equal to that at the reservoir scale. As reported by Sammis et al. (1992), the values of the fractal dimension measured at The Geysers geothermal oil field at different scales, the outcrop, road cut, and regional scales, were almost the same, at least in two dimensions.

Based on the previous studies, we speculated that there may be a relationship between the fractal dimension and the steam production rate in geothermal reservoirs. However this speculation is yet to be studied and verified using production data.

2.7 CONCLUSIONS

Based on the present study, the following conclusions may be drawn:

1. The results demonstrated that the pore systems of the core samples from The Geysers geothermal field are fractal.
2. The fractal technique proposed in this article to characterize the capillary pressure curve of The Geysers rock works satisfactorily. The values of the fractal dimension can be used to represent the heterogeneity of different rock samples quantitatively.
3. The fractal dimension of The Geysers rock was greater than that of Berea sandstone, which implies that The Geysers rock is more heterogeneous.
4. The Geysers rock samples studied have similar features in capillary pressure curves. However the features of The Geysers rock are different from those of Berea sandstone.
5. Unlike Berea sandstone, the capillary pressure curves of The Geysers rock could not be represented using the frequently-used Brooks-Corey model.

3. REFERENCES

Babadagli T. and Develi K.: “Fractal Analysis of Natural and Synthetic Fracture Surfaces of Geothermal Reservoir Rocks,” Proceedings of the World Geothermal Congress, Kyushu-Tohoku, Japan, May 28-June 10, 2000.

Brooks, R.H. and Corey, A.T.: “Hydraulic Properties of Porous Media,” Colorado State University, Hydro paper No.5 (1964).

Brooks, R. H. and Corey, A. T.: "Properties of Porous Media Affecting Fluid Flow", *J. Irrig. Drain. Div*., (1966), 6, 61.

Chen, C.-Y., Diomampo, G., Li, K. and Horne, R.N.: "Steam-Water Relative Permeability in Fractures," *Geothermal Resources Council Transactions Vol.26*, pp. 87-94, 2002.

Corey, A. T.: "The Interrelation between Gas and Oil Relative Permeabilities", *Prod. Mon*., (1954), **19**, 38.

Diomampo, G., "Relative Permeability through Fractures", MS thesis, Stanford University, Stanford, California (2001).

Diomampo, G., Chen, C.-Y, Li, K. and Horne, R.N.: "Relative Permeability through Fractures," *Proc. 27th Workshop on Geothermal Reservoir Engineering*, Stanford University, Stanford, California, January 28-30, 2002.

Fourar, M. and Bories, S.,: "Experimental Study of Air-Water Two-Phase Flow Through a Fracture (Narrow Channel)," *Int. J. Multiphase Flow* Vol. 21, No. 4, (1995) pp. 621-637.

Fourar, M., Bories., Lenormand, R., and Persoff, P.,: "Two-Phase Flow in Smooth and Rough Fractures: Measurement and Correlation by Porous-Medium and Pipe Flow Models," *Water Resources Research* Vol. 29 No. 11. November 1993, pp. 3699-3708.

Horne, R.N., Satik, C., Mahiya, G., Li, K., Ambusso, W., Tovar, R., Wang, C., and Nassori, H.: "Steam-Water Relative Permeability," *Proc. of the World Geothermal Congress* 2000, Kyushu-Tohoku, Japan, May 28-June 10, 2000.

Kneafsy, T. J. and Pruess, K.,: "Laboratory Experiments on Heat-Driven Two-Phase Flows in Natural and Artificial Rock Fractures," *Water Resources Research* Vol. 34, No. 12, December 1998, pp. 3349-3367.

Li, K. and Horne, R.N.: “An Experimental Method for Evaluating Water Injection into Geothermal Reservoirs,” presented at the GRC 2000 annual meeting, September 24-27, 2000, San Francisco, USA; GRC Trans. V. 24 (2000).

Lockhart, R. W. and Martinelli, R.C.,: "Proposed Correction of Data for Isothermal Two-Phase Component Flow in Pipes," *Chem. Eng. Prog*., Vol. 45, No. 39, 1949.

Mahiya, G., “Experimental Measurement of Steam-Water Relative Permeability,” MS thesis, Stanford University, Stanford, California (1999).

Pan, X., Wong, R.C., and Maini, B.B.: Steady State Two-Phase Flow in a Smooth Parallel Fracture, presented at the 47th Annual Technical Meeting of the Petroleum Society in Calgary, Alberta, Canada, June 10-12, 1996.

Persoff, P. K., Pruess, K., and Myer, L.: "Two-Phase Flow Visualization and Relative Permeability Measurement in Transparent Replicas of Rough-Walled Rock Fractures," *Proc. 16th Workshop on Geothermal Reservoir Engineering*, Stanford University, Stanford, California, January 23-25, 1991

Persoff, P., and Pruess, K.: "Two-Phase Flow Visualization and Relative Permeability Measurement in Natural Rough-Walled Rock Fractures," *Water Resources Research* Vol. 31, No. 5, May, 1995, pp. 1175-1186.

Pruess, K., and Tsang, Y. W.: "On Two-Phase Relative Permeability and Capillary Pressure of Rough-Walled Rock Fractures," *Water Resources Research* Vol. 26 No. 9, September 1990, pp 1915-1926.

Purcell, W.R.: "Capillary Pressures-Their Measurement Using Mercury and the Calculation of Permeability", *Trans. AIME,* (1949), 186, 39.

Richardson, J.G., Kerver, J.K., Hafford, J.A., and Osoba, J.S.: "Laboratory Determination of Relative Permeability", *Trans*. *AIME,* (1952), **195**, 187.

Romm, E.S.: "Fluid Flow in Fractured Rocks", “Nedra” Publishing House, Moscow, 1966 (translated from the Russian).

Sammis, C.G., An, L., and Ershaghi, I.: “Determining the 3-D Fracture Structure in the Geysers Geothermal Reservoirs,” Proceedings of 21st Workshop on Geothermal Reservoir Engineering, Stanford, California, 1992.

Scheidegger, A.E. *The Physics of Flow Through Porous Media*, 3rd ed., University of Toronto, Toronto. 1974.

Shen, P. and Li, K.: “A New Method for Determining the Fractal Dimension of Pore Structures and Its Application,” Proceedings of the 10th Offshore South East Asia Conference, Singapore, December 6-9, 1994.

Shen, P. and Li, K.: “Quantitative Description for the Heterogeneity of Pore Structure by Using Mercury Capillary Pressure Curves,” SPE 29996, Proceedings of the SPE International Meeting held in Beijing, China, November 14-17, 1995.

Su, G. W., Geller, J. T., Pruess, K. and Wen, F.,: " Experimental Studies of Water Seepage and Intermittent Flow in Unsaturated, Rough-Walled Fractures," *Water Resources Research*, Vol. 35, No. 4, April 1999, pp. 1019-1037.

Tateno, M., Watanabe, K., Nakatsuka, K., and Takahashi, H.: “Fractal Characterization of the Fracture Distribution and the Permeability in Geothermal Reservoirs,” Proceedings of the World Geothermal Congress, Florence, Italy, May 18-31, 1995.

Tsuchiya, N. and Nakatsuka, K.: “Fractal Analysis and Modeling of a Two-Dimensional Fracture Network,” Proceedings of the GRC 1995 annual meeting, October 8-11, 1995, Reno, USA.

Witherspoon, P.A., Wang, J.S.W., Iwai, K. and Gale, J.E.: " Validity of Cubic Law for Fluid Flow in a Deformable Rock Fracture," *Water Resources Research*, Vol. 16, No. 6, 1980, pp 1016-1024.